HHS Public Access

Author manuscript

*Cell*. Author manuscript; available in PMC 2024 November 09.

Published in final edited form as:

*Cell*. 2023 November 09; 186(23): 5028–5040.e14. doi:10.1016/j.cell.2023.09.021.

# Molecular basis of Wnt biogenesis, secretion and Wnt7 specific signaling

**Xiaofeng Qi**[1,4,*], **Qinli Hu**[1,4], **Nadia Elghobashi-Meinhardt**[2], **Tao Long**[1], **Hongwen Chen**[1], **Xiaochun Li**[1,3,5,*]

[1]Department of Molecular Genetics, University of Texas Southwestern Medical Center, Dallas, TX 75390, USA

[2]School of Chemistry, University College Dublin, South Belfield Dublin 4, Ireland

[3]Department of Biophysics, University of Texas Southwestern Medical Center, Dallas, TX 75390, USA

[4]These authors contributed equally to this work

[5]Lead contact

## Summary:

Wnt proteins are enzymatically lipidated by Porcupine in the ER and bind to Wntless for intracellular transport and secretion. Mechanisms governing the transfer of these low solubility Wnts from the ER to the extracellular space remain unclear. Through structural and functional analyses of Wnt7a, a crucial Wnt involved in central nervous system angiogenesis and blood-brain barrier maintenance, we have elucidated principles of Wnt biogenesis and Wnt7-specific signaling. The Wnt7a-Wntless complex binds to calreticulin revealing that calreticulin functions as a chaperone to facilitate Wnt transfer from Porcupine to Wntless during Wnt biogenesis. Our structures, functional analyses, and molecular-dynamics simulations demonstrate that a phospholipid in the core of Wnt-bound Wntless regulates the association and dissociation between Wnt and Wntless, suggesting a lipid-mediated Wnt secretion mechanism. Finally, the structure of Wnt7a bound to RECK, a cell surface Wnt7 co-receptor, reveals how $RECK^{CC4}$ engages the N-terminal domain of Wnt7a to activate Wnt7-specific signaling.

## Graphical Abstract

*Correspondence: xiaofeng.qi@utsouthwestern.edu (X.Q.) or xiaochun.li@utsouthwestern.edu (X.L.).

Author Contributions

X.Q. initialized the project. X.Q. and Q.H. performed cryo-EM experiments and conducted the biochemical and cell-based signaling assays. N.E.-M performed molecular dynamics simulations. T.L. purified Wnt3a-WLS-CALR complex and H.C. screened the WLS constructs. All authors analyzed the data. X.Q., Q.H. and X.L. designed the research and contributed to manuscript preparation. X.L. conceived the research and wrote the manuscript.



**Declaration of interests** The authors declare no competing interests.

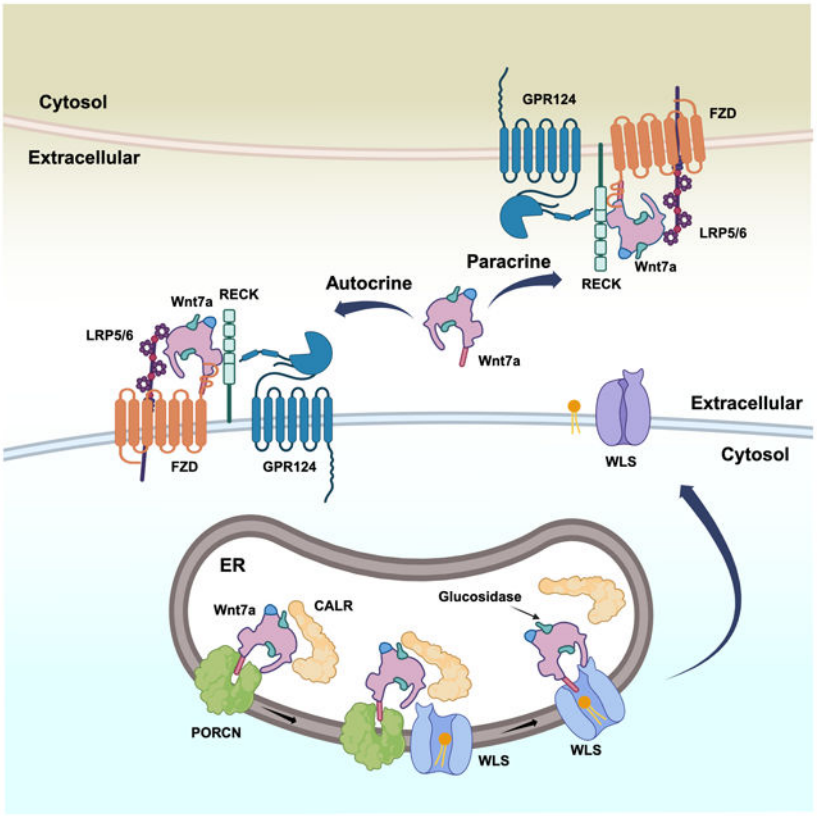


## In brief:

This study demonstrates that calreticulin facilitates the transfer of Wnt from Porcupine to Wntless during Wnt biogenesis and proposes a lipid-mediated Wnt release mechanism, along with the characterization on how Wnt7 co-receptor RECK binds to Wnt7a for ligand-specific signaling.

### Keywords

Wnt; Wntless; Porcupine; calreticulin; N-glycan; RECK; phospholipid; cryo-EM

## Introduction

Wnt signaling is a fundamental signal cascade that plays a crucial role in human development and stemness.[1-4] Aberrant Wnt signaling is frequently and closely linked to various cancers.[5-9] Wnt signaling is triggered by the interactions between the secreted lipid-modified signaling glycoproteins Wnt and their Frizzled (FZD) receptors, as well as their co-receptors.[10-12] Wnt is synthesized in the endoplasmic reticulum (ER) and the ER-resident membrane-bound O-acyltransferase Porcupine (PORCN) transfers a mono-unsaturated palmitoleate moiety (PAM) to a conserved serine residue on the hairpin 2 of Wnt proteins.[13-15] A previous study showed that the palmitoylation is indispensable for Wnt secretion and either mutation of the crucial serine or loss of PORCN activity causes the retention of Wnts in the ER.[16] After lipidation, the membrane protein Wntless (WLS)

employs its extracellular domain and transmembrane region to engage with the modified Wnt.[17] This interaction facilitates Wnt transport across intracellular compartments.[18-20]

Nineteen human Wnt ligands have been identified to activate different signaling pathways through the paracrine and autocrine systems.[21] Human Wnt proteins contain at least 22 cysteine residues, which form multiple disulfide bonds contributing to the stability and folding of Wnts. Lipidated Wnt ligands, owing to their hydrophobic nature, often exhibit low solubility in aqueous environments, therefore necessitating protein partners during Wnt production. The crucial processes of Wnt lipidation and intracellular transport in all metazoans are mediated by two membrane proteins, PORCN and WLS, respectively. This implies the existence of a universal principle governing Wnt production.

One possible model for Wnt secretion involves direct release into the extracellular space. To start, the Wnt-WLS complex moves from the ER to the plasma membrane through the Golgi apparatus (Figure 1A). Once the Wnt-WLS complex reaches the cell surface, Wnt molecules bind to their receptors on the cell that excreted them (autocrine signaling) or to neighboring cells (paracrine signaling). This process may involve the transfer of Wnt molecules to various entities such as cell-surface proteoglycans and soluble transport proteins.[21-23] Another model suggests that the Wnt-WLS complex, after localizing to the plasma membrane, undergoes endocytosis and subsequent dissociation within an endosomal compartment. This then allows the Wnt to be loaded onto exosomes for secretion.[24] Various hypotheses regarding the dissociation of Wnt from WLS have proposed: that low pH regulates Wnt release,[25] that specific lipids compete with the palmitoleoyl moiety of Wnt in WLS,[17,26] or that alterations in membrane curvature promote Wnt release.[24] However, limited experimental evidence supports these proposed mechanisms; therefore, the molecular determinants of Wnt release from WLS remain elusive.

We selected Wnt7a as a Wnt representative to examine the process of Wnt production using biophysical and cell biological approaches. Wnt7 ligands, including Wnt7a and Wnt7b, are crucial for central nervous system (CNS) angiogenesis and the maintenance of blood-brain barrier (BBB) integrity.[27] GPR124 and RECK act as essential co-receptors of Wnt7 for stimulating the ligand-specific canonical Wnt signaling, since an enhanced activation of Wnt signaling is not observed with the other 17 mammalian Wnts or Norrin in the presence of GPR124 and RECK.[28-30] GPR124 contains seven transmembrane helices (TMs) and a >70kD extracellular domain (including a leucine-rich repeat (LRR) domain and Ig-like domain). RECK consists of five repeats of an uncommon domain with six cysteines (the CC domain) and a Frizzled-like cysteine-rich domain (Fz-like CRD), two epidermal growth factor-like domains (EGF-like 1 and 2), and three Kazal-like motifs (Kazal-like 1 to 3).[31] Moreover, low-density lipoprotein receptor-related proteins 5 and 6 (LRP5 and LRP6) activate Wnt signaling as co-receptors of Wnt ligands (Figure S1A).[32,33] Recently, several studies have identified the interaction residues between RECK and Wnt7a and proposed a model of the RECK-Wnt7-FZD-GPR124-LRP5/6 complex[31,34-36]; however, obtaining structural evidence is necessary to reveal the molecular mechanism of Wnt7 signaling by this complex.

Here, we identified calreticulin (CALR) as a glycan chaperone for Wnt proteins in the ER. Our findings also indicate that the incorporation of a phospholipid into WLS enhances the recruitment of Wnt proteins. In the apo state of WLS, the conformation of TMs 6-7 changes, obstructing the binding sites for the central phospholipid in WLS and Wnt protein, suggesting a mechanism by which lipids mediate the release of Wnts. Moreover, we have determined the structure of RECK bound to Wnt7a, revealing that the CC4 domain of RECK is essential for binding Wnt7a to activate the Wnt ligand-specific signal.

## Reconstitution of Wnt7a-WLS complexes

A previous study showed that RECK plays a pivotal role in the Wnt7 signaling process within receiving cells, but it also participates in the biogenesis and/or release of Wnt7 from secreting cells.[37] Thus, we co-expressed human Flag-tagged WLS with C-terminal Strep-tagged Wnt7a and untagged full-length RECK ($RECK^{FL}$) in HEK293 cells to capture how Wnt7a binds to WLS and RECK. The lysate was incubated with anti-Flag M2 resin, and the affinity-purified material was then applied to gel filtration (Figure S1B). Notably, $RECK^{FL}$ can be detected on the SDS-PAGE; however, the stoichiometry of Wnt7a and $RECK^{FL}$ did not appear to be 1:1. Nevertheless, we subjected this sample to cryo-EM analysis and, after 3D classification, obtained two classes of Wnt7a-bound WLS at an overall resolution of 3.2-3.6 Å (Figure S1C). In Class-1, a four-helix bundle binds to the N-terminal domain (NTD) of Wnt7a, while Class-2 exhibits a globular protein bound to the C-terminal domain (CTD) of Wnt7a (Figure S1D). There is no 3D class that concomitantly contains both extra densities, indicating that two different states of the Wnt7a-WLS complex were captured in this dataset and that binding of the two extra ligands is mutually exclusive.

Since the previously determined crystal structure of the mouse RECK CC4 domain ($mRECK^{CC4}$)[31] fits well into the density of the four-helix bundle in the Class-1 map, we speculated that the extra density corresponds to $RECK^{CC4}$, which was previously shown to be vital for the interaction with Wnt7a.[34,35] Since the extra density of Class-2 could not be assigned to a RECK region, we employed mass spectrometry to analyze the purified Wnt7a-WLS complex from the SDS-PAGE. Unexpectedly, an ER glycan-chaperone CALR is present at high abundance in the sample. Since the molecular weights of WLS and CALR are similar, the ~50 kD band represents both proteins (Figure S1B and E). CALR assists in the folding process in the ER and regulates the quality of newly synthesized glycoproteins via binding oligosaccharides with terminal glucose residues before these glycoproteins are transported to different subcellular compartments.[38] Although the AlphaFold-predicted model[39] and previously determined structures[40,41] of CALR could be docked into the density map of Class-2, the interaction details between Wnt7a and CALR were limited owing to the lower local resolution. We used the crosslinker $BS^3$ to increase complex stability for cryo-EM study (Figure S1F). Using this method, we were able to determine the Wnt7a-WLS-CALR complex at 3.1-Å resolution revealing the interface details between Wnt7a and CALR (Figures 1B, S2A-D and Table S1).

By contrast, crosslinking with $BS^3$ did not improve the quality of the interface between Wnt7a and the presumed $RECK^{CC4}$ domain of Class-1. Thus, we co-expressed Wnt7a and WLS without RECK and incubated purified Wnt7a-WLS with recombinant $RECK^{CC4}$

purified from HEK 293 cells. The resulting Wnt7a-WLS-RECK$^{CC4}$ structure was determined at 3.2-Å resolution, confirming our previous finding using full-length RECK that Wnt7a employs its N-terminal domain to recruit RECK$^{CC4}$ (Figures S3A-D and Table S1). In addition, we expressed Flag-tagged human WLS alone from HEK293 cells and obtained the structure of WLS in the apo state at 3.8-Å resolution (Figure S3E-H and Table S1). The overall structure of WLS is at a moderate resolution level, but the side chains of most TMs could be assigned unambiguously (Figure S3H).

## Structure of the Wnt7a-WLS-CALR complex

The conformation of WLS in the Wnt7a-WLS-CALR complex is similar to that in the previously reported Wnt8a-WLS and Wnt3a-WLS complexes[17,26] with Cα R.M.S.D. values of 0.6 Å and 1.1 Å, respectively. The lectin domain of CALR is well resolved in the cryo-EM map, while the P-loop (residues 208-294) and the C-terminal region of Å-helix 3 (residues 378-417) were not built due to the low local resolution (Figures 1B, S2C and S4A-B). Our previous observation on PORCN shows PAM adopting a C shape in the catalytic core of PORCN,[14] whereas in the Wnt7a-WLS complex, PAM presents a more extended conformation, inserted into a cavity between TMs 4-5 of WLS. Several residues (e.g., Ile302, Ile306, and Phe350) are responsible for creating a hydrophobic pocket that accommodates the PAM (Figure 1B). In our complex structure, Wnt7a is well folded, and the CALR binds to its N-glycan at Asn295 and hairpin 3 of the CTD (Figures 1B and S4C).

The high quality of our cryo-EM map allowed us to build a model of the N-glycan of Wnt7a-Asn295 binding to the lectin domain of CALR (Figure 1C). Residues Tyr109, Lys111, Tyr128, Asp135, His145, and Asp 317 of CALR form hydrogen bonds with the sugar moieties of the $Glc_1Man_3$ tetrasaccharide of Wnt7a (Figure 1D).[40] This interaction mode is analogous to that in the complex of CALR and major histocompatibility complex class I (MHC I) in the peptide-loading complex (PLC) (Figure 1E).[42] Moreover, residues 152-157 form β-strand 9 (β9) to interact with the hairpin 3 of Wnt7a, further stabilizing the Wnt7a and CALR complex (Figures 1B and S4B). Another chaperone, ERp57, stabilized the complex of MHC I and CALR through interactions with the end of the P-loop (Figure 1E). In our cryo-EM map at a low threshold, the P-loop in the Wnt7a-WLS-CALR complex contacts the NTD of Wnt7a (Figure S4D-E). Superimposing the complex structure to the PLC shows that ERp57 would clash with Wnt7a, implying that ERp57 is not involved in the Wnt-WLS-CALR complex assembly. It is possible if ERp57 and CALR modulate the Wnt synthesis, then ERp57 might dissociate from Wnt after Wnt is completely synthesized ready for lipidation. Since ERp57 forms a complex with CALR to help glycoprotein folding within the ER lumen,[43] it is also possible that the flexibility of the P-loop in CALR and the co-chaperone ERp57 may not allow this interaction to be fully visualized in the cryo-EM map.

## The role of CALR in Wnt biogenesis

The conservation of the glycosylation sequence, Asn-X-Ser/Thr (X is any amino acid residue except proline), among at least 14 human Wnt proteins is evident in the sequence alignment (Figure S5A). In order to explore whether CALR serves as a general chaperone

during Wnt biogenesis, we co-expressed WLS and different Wnt proteins in HEK293 cells and performed coimmunoprecipitation (Co-IP) assays. Our results showed that the Wnt proteins without the conserved glycosylation site in the CTD, including Wnt8a, Wnt8b, Wnt9a, and Wnt9b, do not bind to CALR (Figure 2A). Interestingly, although there is no glycosylation site in the CTD of Wnt2b, it still associates with CALR (Figure 2A). The sequence alignment and mass spectrometry analysis showed that the residue Asn283 at the NC-linker of Wnt2b is modified with N-glycan and may serve as CALR binding site (Figures. S4F and S5A-B).

To further study the CALR binding mode in the other Wnt proteins, we conducted co-expression experiments involving non-tagged Wnt3a and Flag-tagged WLS in HEK293 cells. The resulting complex was subsequently purified using anti-Flag M2 resin, and crosslinking was achieved using $BS^3$ (Figure S6A). Notably, we obtained a structure of the Wnt3a-WLS-CALR complex at a resolution of 3.5-Å in one of the 3D classes (Figures 2B, S6B-E and Table S1). The local resolution of CALR within the context of the Wnt3a complex was lower than that of Wnt7a, however, it is clear that the N-glycan on Asn298 inserts into the cavity of CALR (Figure 2B). Structural analysis revealed a similar interaction mode between CALR and Wnt3a, as observed in the CALR-Wnt7a complex, but without a contact between β9 of CALR and the hairpin 3 of Wnt3a (Figure 2C-D). These findings strongly suggest that CALR also facilitates the production of other Wnts, albeit with slightly different interaction modes.

To validate the importance of the glycosylation, we individually mutated the glycosylation site of Wnt3a and Wnt7a. When we co-expressed WLS and Wnt variants in HEK293 cells, Co-IP revealed that mutation of the glycosylation site of either Wnt3a or Wnt7a disrupted the interaction between Wnt and endogenous CALR in the Wnt-WLS-CALR complex (Figure 3A and B). Furthermore, the secretion levels of both Wnt3a and Wnt7a variants in HEK293 cells considerably decreased compared to the wild-type Wnts (Figure 3C). Owing to the low secretion yield, the mutations result in reduced autocrine Wnt signaling, underscoring the crucial role of this modification for Wnt production (Figure 3D).

The interaction between CALR and Wnt proteins during the lipidation process catalyzed by PORCN has remained elusive. To shed light on this process, we co-expressed Wnt7a, $PORCN^{L335A}$ (L335A blocks Wnt release thus maintaining the Wnt-PORCN complex,[44] the residue numbering corresponds to the isoform B of PORCN), and CALR in HEK293 cells, followed by purification through gel filtration. Mass spectrometry analysis confirmed the presence of all components in the resulting complex, irrespective of the presence of a crosslinker (Figure S7A-B). While the structural determination of this complex was unsuccessful due to particle heterogeneity, our result strongly suggests the formation of a complex involving Wnt7a, PORCN, and CALR before Wnt is transferred to WLS. Owing to the limited solubility, a direct transfer of lipidated Wnt between PORCN and WLS is unfavorable, but the palmitoleoyl moiety is likely protected by proteins or embedded in the lipid environment. To investigate this transfer, we co-expressed $PORCN^{L335A}$ with Wnt3a or Wnt7a in HEK293 cells. A Co-IP assay showed that endogenous CALR and WLS associate with PORCN when Wnt3a or Wnt 7a is expressed, but no association between PORCN and WLS is detected in the absence of Wnt protein (Figure 3E and F). This finding reveals an

assembly of an intermediate complex comprised of WLS, PORCN, CALR, and Wnt during Wnt modification in ER.

The cryo-EM map of the Wnt7a-WLS-CALR complex visualized two interfaces between Wnt7a and CALR: 1) the N-glycan on Asn295 of Wnt7a interacts with β-strands of CALR (Figure 1D); 2) the NTD of Wnt7a forms a complex with the P-loop of CALR (Figure S4D-E). Our previous molecular dynamics (MD) simulations indicate that the interaction between hairpins 1 and 3 of the Wnt protein and PORCN are highly dynamic.[14] However, in the structure of the Wnt7a-WLS-CALR complex, the hairpins 1 and 3 appear to stably bind to the WLS (Figure 1B). Since hairpin 3 of Wnt presents a flexible nature (Figure S4C), we speculate that the presence of CALR enforces the entire Wnt molecule into a rigid and extended state, thereby facilitating the Wnt-WLS interaction, while hairpin 2 is inserted into PORCN (Figure 3G). After lipidation, hairpin 2 is released from PORCN, and its palmitoleoyl moiety may be embedded in the lipid environment during this transfer to reach the TMs of WLS. The structure of the Wnt7a-WLS-CALR complex shows that the N-glycan on Asn295 becomes the primary binding site for CALR when Wnt7a forms a complex with WLS. It is conceivable that CALR may dissociate from the Wnt7a-WLS complex after ER-resident glucosidases trim the sugar moiety, allowing this complex to traffic to the Golgi. Since there is a high degree of conservation among Wnts, and PORCN, WLS and CALR are conserved across metazoans[17,45] (Figure S4B), our model might be applicable to the majority of Wnt transfers from PORCN to WLS in ER.

## Lipid-mediated Wnt release from WLS

Curiously, we have found a phospholipid density located in the central cavity of WLS, which is open to the extracellular/luminal leaflet of the plasma/ER membrane when it binds to Wnt7a (Figures 4A and S6F). A similar density in this cavity was found in the cryo-EM maps of Wnt8a-WLS and Wnt3a-WLS.[17,26] In our cryo-EM maps of Wnt7a-WLS and Wnt3a-WLS complexes, this density exhibits a distinct shape that closely resembles the characteristics of a phosphocholine molecule but not of any other common phospholipid (Figure S6G). Moreover, the environment of this lipid binding pocket is suitable for the choline head of phosphocholine, so we tentatively assigned the electron density to a 1-palmitoyl-2-oleoyl-glycero-3-phosphocholine (POPC) (Figure 4A and B). In contrast, we did not find an analogous density in the center of apo WLS, potentially due to a decrease in the binding pocket size (Figure 4C). The fatty acid chain of the POPC is directly exposed to the lipid bilayer, implying this association may be regulated by the membrane environment. In the complex, residues Lys238 and Arg303 bind the phosphate group of phosphocholine and the choline head of POPC forms a π-cation interaction with residue Trp234 (Figure 4B). When we mutated Phe230, Trp234, and Phe474, our co-IP assay shows that the interaction between each mutant and Wnt7a is extensively reduced compared to that in wild type (Figure 4D). Notably, these residues are far away from the Wnt binding site, suggesting an important role of POPC in the central cavity for Wnt engagement. A previous work showed that the WLS mutation Y478C reduces the secretion of Wnt3a causing developmental defect in mouse embryos.[46] Our structural analyses show that the hydroxyl group of Y478 forms a hydrogen bond with the side chain of Asn281 to stabilize the central cavity of WLS (Figure 4B).

Compared to the structure of the Wnt7a-WLS complex, the TMs 5-7 of WLS in the apo state undergo a substantial conformational change. The TM7 rotates counterclockwise when viewed from the luminal/extracellular face, pivoting around Met436 (Figure 4E). This conformational change leads the extracellular half of TM7 to move towards the center of WLS, disrupting the POPC and Wnt hairpin 2 binding sites (Figure 4E). TM5 and TM6 in the extracellular leaflet are shifted 3 and 5 Å, respectively, toward the center of WLS. In particular, Phe347 of TM5 rotates by 90° to obstruct the PAM-binding site (Figure 4F). Thus, we term the conformations of WLS in the Wnt7a-bound and apo states as "open" and "closed", respectively. TM5 in the closed conformation narrows the cavity that accommodates PAM in the complex and residues Phe230, Trp234, and Lys238 on TM2 in the closed conformation interfere with binding of the head group of POPC (Figure 4F). The >10-Å movement of the extracellular half of TM7 drastically collapses the cavity that engages the POPC and hairpin 2 of Wnt7a, potentially causing the release of the Wnt ligands (Figure 4F). Importantly, the conformation of WLS in its complexes with Wnt3a, Wnt7a and Wnt8a is quite similar, and the central phospholipid is present in all three complexes.[17,26] Therefore, it is possible that the central phospholipid may control the transition of WLS between the open and closed conformations, further regulating the majority of Wnts' association with and dissociation from WLS.

To test our hypothesis, we conducted MD simulations of the Wnt7a-WLS complex structure (Videos S1-2). The results showed notable differences in the interaction energy between Wnt7a and WLS with and without the POPC. During a 150 ns simulation, we observed that the interaction energy between hairpin 2 and the PAM region of Wnt7a, as well as their neighboring residues within a 3-Å distance, was −72.804 kcal/mol without POPC and −104.661 kcal/mol with POPC (Figure 5A). Similarly, the interaction energy between hairpin 3 of Wnt7a and its neighboring residues within 3-Å distance was −54.136 kcal/mol without POPC and −70.432 kcal/mol with POPC (Figure 5A). Furthermore, our simulations indicated that Phe347 and Phe352 in TM5 exhibited different conformations, illustrating the dynamic behavior of TM5 in the absence of POPC, where it was not bound to the center of WLS (Figure 5B). This conformational variability resulted in a wider cavity that accommodates the PAM region, which aligns with our analysis showing that hairpin 2 and the PAM region of Wnt7a binding to WLS is energetically less stable in the absence of POPC (Figure 5A). Conversely, in the presence of POPC, hydrophobic contacts within the TMs were observed (Figure 4E); as a result, the conformation of TM5 remained stable (Figure 5C). Compared to the results without the POPC, the cavity did not exhibit further opening during the MD simulations (Figure 5B and C). These findings suggest that Wnt tends to dissociate from WLS when the central pocket lacks POPC. This highlights the crucial role of this central lipid in facilitating the interaction between Wnt and WLS.

## Structure of Wnt7a-bound RECK

The structure of the Wnt7a-WLS-RECK$^{CC4}$ complex reveals a substantial interface of over 700 Å$^2$ between Wnt7a and RECK$^{CC4}$ (Figure 6A). RECK$^{CC4}$ is stabilized by three disulfide bonds, and the loop connecting helices 3 and 4 of CC4 (termed L3 loop) plays a crucial role in mediating this interaction (Figure 6B-C). Compared to the previously determined crystal structure of the CC4 domain in the apo state,[31] the L3 loop moves toward

the N-terminal domain of Wnt7a (Figure 6B). Three glutamine residues of CC4 (Gln253 and Gln257 in the L3 loop as well as Gln262 in helix 4) form hydrogen bonds with four residues of Wnt7a, including Gly63, Glu64, Glu89, and Val92 (Figure 6C). Residue Asp244 in helix 3 likely forms a salt bridge with Lys40 of Wnt7a. In addition to these hydrophilic interactions, Pro254/Leu255/Pro256 in the L3 loop contribute hydrophobic contacts with Wnt7a and Ile60 of Wnt7a has hydrophobic interaction with helix 4 (Figure 6C). A disulfide bond (Cys38-Cys52) confers conformational stability to its N-terminal region, ensuring a specific conformation for interaction with $RECK^{CC4}$ (Figure 6C). The residues of Wnt7a that are responsible for $RECK^{CC4}$ recognition are conserved in Wnt7b but not in the other 17 Wnt proteins, highlighting the specificity of the interaction between Wnt7 and RECK (Figure S5A).

To further test our structural findings, we introduced mutations in the full-length Wnt7a and RECK. We mutated Lys40 and Ile60 of Wnt7a to serine and proline respectively, according to the sequence of Wnt3a. Although the secretion yield of these mutants was high, they showed reduced signaling activity (Figure 6D). Each mutation resulted in a reduction of signal activity compared to wild-type RECK, consistent with previous alanine-scanning studies on $RECK^{CC4}$ to map the interface between RECK and Wnt7a (Figure 6E).[35] A previous study purported to show that the NC-linker of Wnt7a (residues 238-266) plays a key role in binding RECK[34], which is inconsistent with our finding (Figures 6A and C and S4C). A more recent study demonstrated that the NC-linker is crucial for binding to $LRP6^{E2}$ domain, which is essential for Wnt7-mediated signaling.[47] Therefore, the NTD of Wnt7a functions as the primary binding site of RECK. Based on our structural findings, we generated a model of CC4-bound Wnt7a using the previously determined structures of the Wnt8-$FZD8^{CRD}$-$LRP6^{E1E2}$ (Figure 6F).[47] This model shows that the interaction between RECK and Wnt7a does not interfere with the Wnt-$FZD^{CRD}$ and Wnt-LRP6 interface. Collectively, our work provides a structural framework for understanding the physiology of Wnt7 signaling and paves the way for further studies on the Wnt ligand-specific signalosome.

## Discussion

Nineteen human Wnt ligands activate various signaling pathways through both paracrine and autocrine signaling mechanisms.[21] Owing to the PAM modification, Wnt is extremely insoluble; therefore, molecular chaperones are required for its production and trafficking. Although its extracellular chaperones (e.g., secreted FZD-related proteins, Swim, and Afamin) have been identified[48-50], its intracellular chaperone(s) have remained unclear. Here, we identify CALR as an intracellular binding partner of Wnts that may function as a general Wnt chaperone for modified Wnt proteins in the lumen of the ER, ensuring their proper folding and transfer between PORCN and WLS (Figure 7). Supported by structural and functional data, we propose a Wnt transferring complex (WTC), consisting of Wnt-PORCN-CALR-WLS, which avoids direct diffusion and the exposure of PAM to the aqueous environment during its ER transport (Figures 3G and 7). The interaction between CALR and Wnt may furthermore serve as a quality control for Wnt production ensuring the efficient transfer from PORCN to WLS, since abolishing the glycosylation site affects Wnt secretion substantially (Figure 3C).

When the Wnt-WLS complex arrives at the plasma membrane, Wnts may directly dissociate from WLS and interact with extracellular chaperones. Alternatively, the complex may be endocytosed into an endosomal compartment, where the released Wnt can bind to another carrier or become embedded in micelles in exosomes for secretion. Our work suggests a lipid-mediated mechanism for Wnt-WLS complex assembly and dissociation (Figure 7). Specifically, we found a phosphocholine in the central cavity of WLS that may play a critical role in the interaction between WLS and Wnt. In the ER membrane, the phosphocholine (PC) concentration exceeds 55% much more than that in plasma membrane (< 20%).[51] These PC levels imply that phosphocholine diffusion into the lipid-binding pocket of WLS is a plausible process in the ER, facilitating Wnt binding. PC release into the plasma membrane may lead to subsequent conformational changes in WLS, ultimately resulting in the release of Wnt into the extracellular space or exosomes. This regulation bears a resemblance to how PIP2 binding triggers the conformational change of the TMs of an ion channel.[52] Additionally, membrane curvature may provide a mechanical force to extrude the lipid, further destabilizing the interactions between Wnt and WLS.[24] It is tempting to speculate that any factors that disrupt the interactions between the central lipid and WLS could accelerate the release of Wnt.

Finally, our findings have implications for interfering with Wnt signaling for therapeutic purposes. Specifically, the apo WLS structure reveals a central pocket within its transmembrane region (Figure 4C) which could be targeted by a small molecule. Such a compound may stabilize WLS in the closed conformation, prevent the lipid-induced conformational change and subsequent recruitment of Wnt proteins. This may reduce Wnt signaling, which would be potentially beneficial for treating Wnt-dependent tumors.

## Limitations of the study

Owing to the transient interactions between PORCN, Wnt, CALR and WLS, we were not able to capture the structure of this intermediate state. Other approaches, e.g., signal molecule fluorescence and *in situ* cryo-electron tomography, may be required. Moreover, our cryo-EM map suggests that phosphocholine binds to the center of WLS and regulates its interaction with Wnt. We attempted to identify this lipid using mass spectrometry; however, phospholipid is highly abundant in the lipid bilayer and consistently associates with membrane proteins, making it impossible to distinguish this lipid unambiguously. There it is possible that an alternative lipid species resides within the core of WLS, exerting influence over the regulation of Wnt release. While the specific kind of the lipid may not markedly affect our proposed lipid-mediated Wnt secretion mechanism, further work is required to refine this model.

## STAR★Methods

### RESOURCE AVAILABILITY

**Lead contact—**Further information and requests for resources and reagents should be directed to and will be fulfilled by the lead contact, Xiaochun Li (xiaochun.li@utsouthwestern.edu).

**Materials availability—**Plasmids generated in this study and the raw cryo-EM dataset are available upon request from the lead contact.

### Data and code availability

- The 3D cryo-EM density maps have been deposited in the Electron Microscopy Data Bank (EMDB) under the accession numbers EMD-41764, EMD-41765, EMD-41767 and EMD-41768. Atomic coordinates for the atomic model have been deposited in the Protein Data Bank (PDB) under the accession numbers 8TZ0, 8TZP, 8TZR and 8TZS.
- This paper does not report original code.
- Any additional information required to reanalyze the data reported in this paper is available from the lead contact upon request.

## Experimental Model and Study Participant Details

**Cell lines—***Spodoptera frugiperda* Sf9 cells (ATCC) were used to generate baculovirus and maintained in Sf-900 III SFM medium (Gibco) at 27°C with shaking. HEK 293S GnTI$^-$ cells (ATCC) were used for protein expression and co-immunoprecipitation assays and maintained in Freestyle 293 expression medium (Gibco) at 37°C and 8% $CO_2$ with shaking. SuperTopFlash HEK293 (293STF, ATCC) were used for Wnt signaling assays and maintained in DMEM/F12 50/50 Mix medium (Corning) at 37°C in a humidity and $CO_2$ controlled incubator.

## METHOD DETAILS

### Protein expression and purification

**WLS alone, WLS-Wnt7a, WLS-Wnt3a and WLS-Wnt7a-RECK$^{FL}$ complexes:** The complementary DNA (cDNA) encoding human WLS was cloned into the pEZT-BM vector with a C-terminal Flag tag. The cDNA encoding human Wnt7a was cloned into pEG BacMam vector with a GG linker followed by a Strep tag or a 6xHis tag at the C-terminus. The cDNA encoding human Wnt3a was cloned into the pEZT-BM vector without a tag. The cDNA encoding human RECK was cloned into pEG BacMam vector without a tag. Site-directed mutagenesis was carried out by QuikChange II kit (Agilent) or two-step overlapping PCR. All proteins were expressed using baculovirus-mediated transduction of mammalian HEK 293 S GnTI$^-$ cells (ATCC). Baculoviruses were produced by transfecting Sf9 cells with the bacmids using Cellfectin II (Gibco). Totally 50 ml P2 baculoviruses were used to infect 1 L HEK293S GnTI$^-$ at a density of 2-3 × $10^6$ cells/ml. For WLS-Wnt7a or WLS-Wnt3a complex, the volume ratio of baculoviruses of WLS and Wnt7a (Strep tagged)/Wnt3a is 1:4. For WLS-Wnt7a-RECK$^{FL}$ complex, the volume ratio of baculoviruses of WLS, Wnt7a (6xHis tagged) and RECK is 1:4:1.5. 8 h after infection, 10 mM sodium butyrate was supplemented to the cells, and the cells was moved to 30 °C. For WLS-Wnt7a, WLS-Wnt3a and WLS-Wnt7a-RECK$^{FL}$ complexes, 20 nM Bafilomycin A1 (Fisher Scientific) was added to the cells with sodium butyrate. Cells were collected at 72 h post-infection for protein purification.

The pellet from 1L cells was resuspended in 20 ml buffer A (20 mM HEPES, 150 mM NaCl, pH 7.5) supplemented by 10 μg $ml^{-1}$ leupeptin, 1 mM Phenylmethylsulfonyl fluoride (PMSF) and disrupted by sonication. After low-speed centrifugation, the resulting supernatant was then incubated with 1% (w/v) lauryl maltose neopentyl glycol (LMNG, Anatrace) at 4 °C for 1 h. The insoluble fraction was removed by centrifugation (20,000g, 4°C, 30 min), and the supernatant was incubated with 1 ml anti-Flag M2 resin (Sigma Aldrich) at 4 °C for 1 h. The beads were then washed with 20 column volume (CV) buffer B (20 mM HEPES, 150 mM NaCl, 0.01% LMNG, pH 7.5) by gravity flow. Proteins were eluted in 5 CV buffer B supplemented by 100 μg $ml^{-1}$ 3×Flag peptide. The eluate was concentrated and further purified by size-exclusion chromatography (SEC) (Superose 6 Increase, 10/300 GL column, GE Healthcare) in buffer C (20 mM HEPES, 150 mM NaCl, 0.06% digitonin, pH 7.5) for cryo-EM or crosslinking studies. For WLS-Wnt7a-$RECK^{FL}$ complex, an additional cryo-EM sample was prepared in buffer A supplemented 0.003% glycol-diosgenin (GDN).

**$RECK^{CC4}$ protein:** The cDNA encoding human $RECK^{CC4}$ (206-270) was cloned to pHL-sec vector which contains a N-terminal signal peptide and C-terminal 6xHis tag. 0.6 mg plasmid was transfected to 0.5 L HEK293S $GnTI^{-1}$ cells by 1.6 mg PEI Max (Polysciences) for protein expression. The medium was collected at 72 h post-transfection/infection and loaded on the Ni-NTA and flowed through by gravity. The Ni-NTA was then washed with 20 CV buffer A containing 20 mM imidazole by gravity flow. Proteins were eluted in 5 CV buffer A containing 250 mM imidazole. The eluate was concentrated and further purified by SEC (Superdex® 200 Increase, 10/300 GL column, GE Healthcare) in buffer A for complex assembly.

**$PORCN^{L335A}$-Wnt7a-CALR complex:** The cDNA encoding human PORCN (isoform B) and containing a L335A mutation was cloned into the pEG-BacMam vector with a N-terminal Flag tag. The cDNA encoding human calreticulin (CALR) was cloned into pEG BacMam vector with a C-terminal 8xHis tag. Baculoviruses were produced as described above. The volume ratio of P2 baculoviruses for infection of $PORCN^{L335A}$, Wnt7a (Strep tagged) and CALR is 3:7:2. After 8 h, 10 mM sodium butyrate was supplemented to the cultures, and the cells was moved to 30 °C. Cells were collected at 72 h post-infection for protein purification.

The pellet of 1 L post-transduction cells was resuspended in 20 ml buffer A supplemented by 10 μg $ml^{-1}$ leupeptin, 1 mM PMSF and disrupted by sonication. After low-speed centrifugation, the resulting supernatant was then incubated with 1% (w/v) LMNG at 4 °C for 1 h. The insoluble fraction was removed by centrifugation (20,000g, 4 °C, 30 min), and the supernatant was incubated for 1 h with 1 ml anti-Flag M2 resin at 4 °C. The beads were then washed with 20 CV buffer B supplemented by 10 μg $ml^{-1}$ 1-palmitoyl-2-oleoyl-sn-glycero-3 -phospho-l-serine (POPS, Anatrace) by gravity flow. Proteins were eluted in 5 CV buffer B supplemented by 100 μg $ml^{-1}$ 3×Flag peptide. The eluate was concentrated and purified by SEC (Superose 6 Increase, 10/300 GL column, GE Healthcare) in buffer C.

**Crosslinking of WLS-Wnt7a-CALR, WLS-Wnt3a-CALR and $PORCN^{L335A}$-Wnt7a-CALR complex:** The purified WLS-Wnt7a-$RECK^{FL}$ complex and WLS-Wnt3a complex

samples, containing endogenous CALR which forms a complex with ER located WLS-Wnt7a/Wnt3a, were incubated with 2 mM $BS^3$ (Thermo Scientific) at 4 °C for 1.5 h, respectively. For $PORCN^{L335A}$-Wnt7a-CALR complex, the purified $PORCN^{L335A}$-Wnt7a-CALR complex was incubated with 5 mM Glutaraldehyde at 4 °C for 3 h. The crosslinking reaction was quenched by 20 mM Tris-HCl, pH 7.5 at room temperature for 10 min. The crosslinked complexes were further purified by SEC (Superose 6 Increase, 10/300 GL column, GE Healthcare) in buffer C.

**Cryo-EM sample preparation and data acquisition:** For WLS-Wnt7a-$RECK^{FL}$/WLS-Wnt7a-CALR (Digitonin, non-crosslinking), WLS-Wnt7a-$RECK^{FL}$/WLS-Wnt7a-CALR (GDN, non-crosslinking), WLS-Wnt7a-$RECK^{FL}$/WLS-Wnt7a-CALR (crosslinked), WLS-Wnt3a-CALR (crosslinked) complexes, Protein samples were concentrated to 5-10 mg $ml^{-1}$ for grid preparation. For WLS-Wnt7a-$RECK^{CC4}$ complex, the purified WLS-Wnt7a and $RECK^{CC4}$ were mix at 1:3 molar ratio and concentrated to 5-10 mg $ml^{-1}$ for grid preparation. For apo WLS, the protein was concentrated to 10-15 mg $ml^{-1}$ for grid preparation. Aliquots of 3 μl protein samples were applied to glow discharged Quantifoil R1.2/1.3 400 mesh Au holey carbon grids (Quantifoil). The grids were blotted and plunged into liquid ethane using a Vitrobot Mark IV (FEI) and loaded onto a 300 kV Titan Krios transmission electron microscope for data collection. For apo WLS, raw movie stacks were collected with a Falcon 4i camera at 0.738 Å per pixel and a nominal defocus range of −0.8 to −1.8 μm. The exposure time for each micrograph was 4 s with a total dose of ~60 electrons per $Å^2$. For other samples, raw movie stacks were collected with a K3 camera at 0.83 Å per pixel and a nominal defocus range of −1to −2 μm. The exposure time for each micrograph was 5 s, dose-fractionated into 50 frames with a total dose of ~60 electrons per $Å^2$.

**Cryo-EM Data Processing:** For apo WLS, motion correction and contrast transfer function (CTF) estimation were performed using cryoSPARC.[53] For other data sets, motion correction was performed using MotionCor2[54] and performed in RELION-3.[54,55] The CTF was estimated using CTFFIND4.[56] For all data sets, Particle picking was performed with crYOLO using the general model.[57] Subsequent 2D classification, ab-initio, heterogenous 3D refinement, non-uniform refinement, CTF refinement, local 3D refinement and particle subtraction were performed in cryoSPARC. For WLS-Wnt7a-$RECK^{FL}$/WLS-Wnt7a-CALR (Digitonin, non-crosslinking) data set, 2D classes with clean background were selected to generate initial models for the heterogenous 3D refinement. The best 3D class showing features of WLS, Wnt7a and two extra densities was subjected to non-uniform refinement. The WLS-Wnt7a-$RECK^{FL}$/WLS-Wnt7a-CALR (GDN, non-crosslinking) data set was processed in a similar way. The final particles from these two data sets were combined and 3D classified in RELION-3 without alignment. The resulting good maps show either a 4-helix bundle like extra density (3D Class-1) or a globular protein like extra density (3D Class-2) (Figure S1C-D). For WLS-Wnt7a-$RECK^{FL}$/WLS-Wnt7a-CALR (crosslinked) data set. Two good models (3D Class-1 and 2) and three bad models from the non-crosslinking data sets were used for heterogenous 3D refinement. The best 3D class containing the CALR density was selected for the non-uniform refinement, CTF refinement and local refinement (Figure S2A). For WLS-Wnt7a-$RECK^{CC4}$ data set, the same five models were

used for heterogenous 3D refinement. The best 3D class containing the RECK$^{CC4}$ density was selected for the further heterogenous 3D refinement, non-uniform refinement, CTF refinement and local refinement (Figure S3A). For WLS-Wnt3a-CALR (crosslinked) data set, good classes in the initial 2D classification were selected to generate initial models for the heterogenous 3D refinement. The best 3D class was selected for the secondary 2D classification and heterogenous 3D refinement, followed by the further heterogenous 3D refinement, non-uniform refinement, CTF refinement and local refinement (Figure S6B). For apo WLS data set, good classes in the initial 2D classification were selected to generate three initial models for four rounds of heterogenous 3D refinement. The resulting best class was subjected to non-uniform refinement and local refinement, followed by the particle subtraction to remove the signal of the detergent micelle. The final local refinement was performed with a mask covering the WLS protein (Figure S3E). For all data sets, the mask-corrected FSC curves were calculated in cryoSPARC. and reported resolutions are based on the 0.143 criterion. Local resolution estimations were performed in cryoSPARC.

**Model building and refinement—**For WLS-Wnt7a-CALR complex, WLS structures from PDB: 7KC4 ,AlphaFold2[39] predicted structures of human Wnt7a and CALR, N-Glycans structure from 7QPD, POPC and PAM structures generated by Phenix[58] were docked into the cryo-EM map as an initial model. For WLS-Wnt7a-RECK$^{CC4}$ complex, WLS, Wnt7a, N-Glycans, POPC and PAM structures from WLS-Wnt7a-CALR complex and AlphaFold2 predicted structure of human RECK$^{CC4}$ (209-270) were docked into the cryo-EM map as an initial model. For WLS-Wnt3a-CALR complex, WLS-Wnt3a structure from PDB: 7DRT, CALR, N-Glycans, POPC and PAM structures from WLS-Wnt7a-CALR complex were docked into the cryo-EM map as an initial model. For apo WLS, WLS structure from WLS-Wnt7a-CALR complex were docked into the cryo-EM map as an initial model. For all structures, the models were manual build in Coot[59] and refined by Phenix and ISOLDE[60] in ChimeraX.[61] In WLS-Wnt7a-CALR and WLS-Wnt7a-RECK$^{CC4}$ complexes, residues 1-36 and 134-145 in Wnt7a, residues 1-2 and 499-541 in WLS were not build. In WLS-Wnt3a-CALR complex, residues 1-39 in Wnt3a, residues 1-2 and 495-541 in WLS were not build. In WLS-Wnt7a-CALR and WLS-Wnt3a-CALR complexes, residues 1-17, 208-294 and 378-417 in CALR were not build. In apo WLS, residues 1-2, 414-418, 457-467 and 499-541 in WLS were not build. Structural model validation was performed using Phenix. Figures were prepared using PyMOL, Chimera[62] and ChimeraX.

**Construction of model—**The Wnt-WLS complex structure was modeled as follows. The atomic coordinates were constructed from Wnt7a-WLS-CALR complex. For the PAM ligand, the hydrogen atoms were constructed using Avogadro (http://avogadro.cc/); the force field parameters were obtained using the CGenFF server.[63] Hydrogen atoms were added to the protein molecules using H-build from CHARMM.[64] An initial protonation pattern at pH 7 was obtained by calculating the pKa values of all titratable residues. For this, electrostatic energy computations were carried out with PROPKA.[65] The following thirteen disulfide bonds were constructed: in Wnt7a Cys38-Cys52, Cys73-Cys84, Cys123-Cys131, C133-C152, Cys200-Cys214, Cys202-Cys209, Cys278-Cys309, Cys294-Cys304, Cys308-Cys348, Cys324-Cys339, Cys326-Cys336, Cys331-Cys332; in WLS, Cys50-Cys71 and Cys162-Cys179.

Next, using the CHARMM-GUI[66] and OPM database[67] the protein complex was inserted in a lipid bilayer consisting of a cytosolic leaflet and an extracellular leaflet. The WLS-Wnt7a complex was simulated in the plasma membrane (PM) in which both leaflets contain 40% cholesterol. In the cytosolic leaflet, the remainder is comprised of 20% 3-palmitoyl-oleoyl-D-glycero-1-Phosphatidylethanolamine (POPE), 20% 3-palmitoyl-2-oleoyl-D-glycero-1-Phosphatidylserine (POPS), and 20% 3-palmitoyl-2-oleoyl-D-glycero-1-phosphatidylinositol (POPI); the extracellular leaflet contains 30% sphingomyelin and 30% palmitoyl-2-oleoyl-D-glycero-1-Phosphatidylcholine (POPC). The protein-membrane system was next solvated in explicit TIP3 water molecules[68] with 150 mM KCl concentration to neutralize charge. The total system was simulated in a rectangular box of dimension ~100 Å × ~100 Å × ~163 Å.

**Geometry optimizations and molecular dynamics—**The initial geometry of each solvated protein-membrane complex was optimized with a combination of 1500 steps of steepest descent (SD) energy minimization and 1500 adopted basis Newton-Raphson (ABNR) steps to remove any close contacts. Energy minimizations and geometry optimizations were carried out with NAMD[69] using the all-atom CHARMM36 parameter set for the protein and lipid molecules,[70] the TIP3P model for water molecules,[68] and the PAM force field parameters as obtained in the previous step using the CGenFF server.[63]

The solvated ligand-protein-membrane complex was simulated with molecular dynamics (MD) at 310 K according to the following protocol: 1) equilibration MD with Langevin dynamics (time step of 1 fs) for 50 ps followed by CPT dynamics (time step 2 fs) for 350 ps; 2) production MD with CPT dynamics (time step 2 fs) for 150 ns. To simulate a continuous system, periodic boundary conditions were applied. Electrostatic interactions were summed with the Particle Mesh Ewald method[71] (grid spacing ~0.92.; fftx 108, ffty 108, fftz 180). A nonbonded cutoff of 12.0 was used.

**Interaction energy calculations—**Interaction energies (electrostatic and van der Waal energies) between amino acids were calculated using the INTER module in CHARMM with the CHARMM36 parameter set. The energies were tabulated at regular intervals of the 150 ns simulation and averaged. Amino acids within a 3 Å radius were selected for two regions of Wnt7a: residues 195-219 including PAM, and residues 327-336.

**Co-Immunoprecipitation—**For endogenous CALR co-immunoprecipitation with WLS-Wnt complex by anti-Flag M2 resin, HEK293S GnTI$^-$ cells were co-infected with P2 baculoviruses of WLS and Wnt7a (Strep tagged), Wnt7a N295T mutant (Strep tagged), other Wnts or their variants (Strep-HA tagged) or empty pEZT-BM vector. For endogenous CALR co-immunoprecipitation with PORCN$^{L335A}$-Wnt7a/Wnt3a complex by anti-Flag M2 resin, HEK293S GnTI$^-$ cells were co-infected with P2 baculoviruses of PORCN$^{L335A}$ and Wnt7a (Strep tagged) or Wnt3a (Strep-HA tagged) or empty pEZT-BM vector. Expression and purification of WLS-Wnt7a and PORCN$^{L335A}$-Wnt7a complexes were performed as described above with a small scale. For Wnt7a co-immunoprecipitation with WLS variants by anti-Flag M2 resin, HEK293S GnTI$^-$ cells were co-infected with P2 baculoviruses of Wnt7a (Strep tagged) and WLS wild-type or mutants. Expression of WLS-Wnt7a complex was performed as described above with a small scale but without adding Bafilomycin A1.

Anti-Flag M2 resin was used for the purification. The Flag-tagged recombined WLS and PORCN$^{L335A}$, Strep-tagged recombined Wnt7a, Strep-HA tagged Wnt3a (Figure 3A and 3E), Strep-HA tagged Wnts (Figure 2A), endogenous CALR and endogenous WLS were detected by western blot using anti-Flag antibody (MBL International, Cat# M185-3L), anti-Wnt 7a antibody (Abcam, Cat# ab274321), anti-Wnt3a antibody (Cell Signaling Technology, Cat# 2721S), anti-HA antibody (Cell Signaling Technology, Cat# 3724S), anti-CALR antibody (Cell Signaling Technology, Cat# 12238S) and anti-WLS (GPR177) antibody (Thermo Scientific, Cat# 50-173-1894), respectively. The endogenous Calnexin (CNX) was used as an internal control and detected by an anti-CNX antibody (Cell Signaling Technology, Cat# 2433S). Each experiment was performed at least three times with similar results.

**Wnt signaling assay—**Wnt signaling activities were measured by Dual-Luciferase® Reporter Assay System (Promega) using SuperTopFlash HEK293 (293STF, ATCC) cells. The pRL-SV40 *Renilla* luciferase (Promega) was used as a control to normalize the signal. Human Frizzled-4 and GPR124 were cloned to pcDNA3.1 vector with a C-terminal Flag tag, respectively. Human Wnt3a and Wnt7a were cloned to pcDNA3.1 vector with a C-terminal GG linker followed by a Strep tag, respectively. Human LRP6 (20-1613) was cloned to pHL-sec vector. Human RECK was cloned to pcDNA3.1 vector without a tag. Site-directed mutagenesis was carried out by QuikChange II kit (Agilent) or two-step overlapping PCR. For signaling assay, the 293STF cells were setup in 24-well plates and transfected by FuGENE6 Transfection Reagent (Promega). To measure the signaling activity of Wnt3a variants, the cells were co-transfected with pRL-SV40 *Renilla* luciferase (20 ng/well), Frizzled-4 (60 ng/well), LRP6 (60 ng/well) and pcDNA3.1 or Wnt3a$^{WT}$ or Wnt3a$^{N298T}$ (20 ng/well). To measure the signaling activity of Wnt7a variants, the cells were co-transfected with pRL-SV40 *Renilla* luciferase (20 ng/well), Frizzled-4 (60 ng/well), LRP6 (60 ng/well), RECK (60 ng/well), GPR124 (60 ng/well) and pcDNA3.1 or Wnt7a$^{WT}$ or Wnt7a$^{N295T}$ (20 ng/well). To measure the signaling activity of RECK or Wnt7a variants, the cells were co-transfected with pRL-SV40 *Renilla* luciferase (20 ng/well), Frizzled-4 (60 ng/well), LRP6 (60 ng/well), GPR124 (60 ng/well), Wnt7a wild-type or Wnt7a mutants (20 ng/well) and pcDNA3.1 or RECK wild-type or RECK mutants (60 ng/well). The Dual-Luciferase assays were performed 48 h post-transfection. The Wnt7a, Wnt3a and RECK in the cells were detected by western-blot using anti-Wnt 7a antibody (Abcam, Cat# ab274321), anti-Wnt 3a antibody (Cell Signaling Technology, Cat# 2721S) and anti-RECK antibody (Thermo Scientific, Cat# MA5-14781). CNX was used as an internal control and detected by an anti-CNX antibody (Cell Signaling Technology, Cat# 2433S). Data analysis was performed using Prism 9 (GraphPad Software). Results are shown as mean±s.d. from three biologically independent experiments. To detect the protein level of Wnt3a/7a variants in the medium, 293STF cells were setup in 10 cm dish and transfected with Wnt3a/7a variants (10 ug/dish) by FuGENE6. 48 h post-transfection, the medium was collected and incubated with Blue Sepharose resin (GE Healthcare) over night to enrich Wnt proteins. The resin was then washed three times with buffer B and the protein was eluted by buffer B supplemented with 1M NaCl for western blot. Wnt3a and Wnt7a were detected by the antibodies mentioned above. Each experiment was performed at least three times with similar results.

**Reproducibility—**All functional experiments were repeated at least three times on different days. Similar results were obtained.

### QUANTIFICATION AND STATISTICAL ANALYSIS

Statistical analyses of data were performed using GraphPad Prism 9. Quantification methods and tools used are described in each relevant section of the methods or figure legends.

## Supplementary Material

Refer to Web version on PubMed Central for supplementary material.

## Acknowledgments

As previous Life Sciences Research Foundation (LSRF) fellows, X.Q. and X.L. conducted this research in memory of Donald D. Brown for his unwavering dedication to LSRF. The Cryo-EM data were collected at the UT Southwestern Medical Center Cryo-EM Facility (CPRIT Core Facility Support Award RP170644). We thank L. Esparza, Y. Qin and L. Beatty for technical support, A. Lemoff at the UTSW Proteomics Core for mass spectrometry analysis, M. Brown for suggestions, and E. Debler, P. Shmiege for editing the manuscript. This work was supported by NIH P01 HL160487, R01 GM135343, the Damon Runyon Cancer Research Foundation (DRR-53S-19) and Welch Foundation (I-1957) (to X.L.). X.Q. was a recipient of DDBrown Fellowship of LSRF.

## Inclusion and diversity

We support inclusive, diverse, and equitable conduct of research.

## References:

1. Nusse R, and Clevers H (2017). Wnt/beta-Catenin Signaling, Disease, and Emerging Therapeutic Modalities. Cell 169, 985–999. 10.1016/j.cell.2017.05.016. [PubMed: 28575679]
2. Willert K, Brown JD, Danenberg E, Duncan AW, Weissman IL, Reya T, Yates JR 3rd, and Nusse R (2003). Wnt proteins are lipid-modified and can act as stem cell growth factors. Nature 423, 448–452. 10.1038/nature01611. [PubMed: 12717451]
3. Taipale J, and Beachy PA (2001). The Hedgehog and Wnt signalling pathways in cancer. Nature 411, 349–354. 10.1038/35077219. [PubMed: 11357142]
4. MacDonald BT, Tamai K, and He X (2009). Wnt/beta-catenin signaling: components, mechanisms, and diseases. Developmental cell 17, 9–26. 10.1016/j.devcel.2009.06.016. [PubMed: 19619488]
5. Zhan T, Rindtorff N, and Boutros M (2017). Wnt signaling in cancer. Oncogene 36, 1461–1473. 10.1038/onc.2016.304. [PubMed: 27617575]
6. Boumahdi S, and de Sauvage FJ (2020). The great escape: tumour cell plasticity in resistance to targeted therapy. Nature reviews. Drug discovery 19, 39–56. 10.1038/s41573-019-0044-1. [PubMed: 31601994]
7. Zhao Y, Ren J, Hillier J, Lu W, and Jones EY (2020). Antiepileptic Drug Carbamazepine Binds to a Novel Pocket on the Wnt Receptor Frizzled-8. Journal of medicinal chemistry 63, 3252–3260. 10.1021/acs.jmedchem.9b02020. [PubMed: 32049522]
8. Zhong Z, Sepramaniam S, Chew XH, Wood K, Lee MA, Madan B, and Virshup DM (2019). PORCN inhibition synergizes with PI3K/mTOR inhibition in Wnt-addicted cancers. Oncogene 38, 6662–6677. 10.1038/s41388-019-0908-1. [PubMed: 31391551]
9. O'Brien S, Chidiac R, and Angers S (2023). Modulation of Wnt-beta-catenin signaling with antibodies: therapeutic opportunities and challenges. Trends in pharmacological sciences 44, 354–365. 10.1016/j.tips.2023.03.008. [PubMed: 37085400]
10. Janda CY, Waghray D, Levin AM, Thomas C, and Garcia KC (2012). Structural basis of Wnt recognition by Frizzled. Science 337, 59–64. 10.1126/science.1222879. [PubMed: 22653731]

11. Hirai H, Matoba K, Mihara E, Arimori T, and Takagi J (2019). Crystal structure of a mammalian Wnt-frizzled complex. Nature structural & molecular biology 26, 372–379. 10.1038/s41594-019-0216-z.
12. Nile AH, and Hannoush RN (2019). Fatty acid recognition in the Frizzled receptor family. The Journal of biological chemistry 294, 726–736. 10.1074/jbc.REV118.005205. [PubMed: 30530496]
13. Zhai L, Chaturvedi D, and Cumberledge S (2004). Drosophila wnt-1 undergoes a hydrophobic modification and is targeted to lipid rafts, a process that requires porcupine. The Journal of biological chemistry 279, 33220–33227. 10.1074/jbc.M403407200. [PubMed: 15166250]
14. Liu Y, Qi X, Donnelly L, Elghobashi-Meinhardt N, Long T, Zhou RW, Sun Y, Wang B, and Li X (2022). Mechanisms and inhibition of Porcupine-mediated Wnt acylation. Nature 607, 816–822. 10.1038/s41586-022-04952-2. [PubMed: 35831507]
15. Resh MD (2012). Targeting protein lipidation in disease. Trends Mol Med 18, 206–214. 10.1016/j.molmed.2012.01.007. [PubMed: 22342806]
16. Takada R, Satomi Y, Kurata T, Ueno N, Norioka S, Kondoh H, Takao T, and Takada S (2006). Monounsaturated fatty acid modification of Wnt protein: its role in Wnt secretion. Developmental cell 11, 791–801. 10.1016/j.devcel.2006.10.003. [PubMed: 17141155]
17. Nygaard R, Yu J, Kim J, Ross DR, Parisi G, Clarke OB, Virshup DM, and Mancia F (2021). Structural Basis of WLS/Evi-Mediated Wnt Transport and Secretion. Cell 184, 194–206 e114. 10.1016/j.cell.2020.11.038. [PubMed: 33357447]
18. Banziger C, Soldini D, Schutt C, Zipperlen P, Hausmann G, and Basler K (2006). Wntless, a conserved membrane protein dedicated to the secretion of Wnt proteins from signaling cells. Cell 125, 509–522. 10.1016/j.cell.2006.02.049. [PubMed: 16678095]
19. Bartscherer K, Pelte N, Ingelfinger D, and Boutros M (2006). Secretion of Wnt ligands requires Evi, a conserved transmembrane protein. Cell 125, 523–533. 10.1016/j.cell.2006.04.009. [PubMed: 16678096]
20. Goodman RM, Thombre S, Firtina Z, Gray D, Betts D, Roebuck J, Spana EP, and Selva EM (2006). Sprinter: a novel transmembrane protein required for Wg secretion and signaling. Development 133, 4901–4911. 10.1242/dev.02674. [PubMed: 17108000]
21. Routledge D, and Scholpp S (2019). Mechanisms of intercellular Wnt transport. Development 146. 10.1242/dev.176073.
22. Stapornwongkul KS, and Vincent JP (2021). Generation of extracellular morphogen gradients: the case for diffusion. Nat Rev Genet 22, 393–411. 10.1038/s41576-021-00342-y. [PubMed: 33767424]
23. Waghmare I, and Page-McCaw A (2022). Regulation of Wnt distribution and function by Drosophila glypicans. Journal of cell science 135. 10.1242/jcs.259405.
24. Alvarez-Rodrigo I, Willnow D, and Vincent JP (2023). The logistics of Wnt production and delivery. Curr Top Dev Biol 153, 1–60. 10.1016/bs.ctdb.2023.01.006. [PubMed: 36967191]
25. Coombs GS, Yu J, Canning CA, Veltri CA, Covey TM, Cheong JK, Utomo V, Banerjee N, Zhang ZH, Jadulco RC, et al. (2010). WLS-dependent secretion of WNT3A requires Ser209 acylation and vacuolar acidification. Journal of cell science 123, 3357–3367. 10.1242/jcs.072132. [PubMed: 20826466]
26. Zhong Q, Zhao Y, Ye F, Xiao Z, Huang G, Xu M, Zhang Y, Zhan X, Sun K, Wang Z, et al. (2021). Cryo-EM structure of human Wntless in complex with Wnt3a. Nature communications 12, 4541. 10.1038/s41467-021-24731-3.
27. Wang Z, Liu CH, Huang S, and Chen J (2019). Wnt Signaling in vascular eye diseases. Prog Retin Eye Res 70, 110–133. 10.1016/j.preteyeres.2018.11.008. [PubMed: 30513356]
28. Zhou Y, and Nathans J (2014). Gpr124 controls CNS angiogenesis and blood-brain barrier integrity by promoting ligand-specific canonical wnt signaling. Developmental cell 31, 248–256. 10.1016/j.devcel.2014.08.018. [PubMed: 25373781]
29. Ulrich F, Carretero-Ortega J, Menendez J, Narvaez C, Sun B, Lancaster E, Pershad V, Trzaska S, Veliz E, Kamei M, et al. (2016). Reck enables cerebrovascular development by promoting canonical Wnt signaling. Development 143, 147–159. 10.1242/dev.123059. [PubMed: 26657775]

30. Cho C, Smallwood PM, and Nathans J (2017). Reck and Gpr124 Are Essential Receptor Cofactors for Wnt7a/Wnt7b-Specific Signaling in Mammalian CNS Angiogenesis and Blood-Brain Barrier Regulation. Neuron 95, 1056–1073 e1055. 10.1016/j.neuron.2017.07.031. [PubMed: 28803732]

31. Chang TH, Hsieh FL, Smallwood PM, Gabelli SB, and Nathans J (2020). Structure of the RECK CC domain, an evolutionary anomaly. Proceedings of the National Academy of Sciences of the United States of America 117, 15104–15111. 10.1073/pnas.2006332117. [PubMed: 32541044]

32. Tamai K, Semenov M, Kato Y, Spokony R, Liu C, Katsuyama Y, Hess F, Saint-Jeannet JP, and He X (2000). LDL-receptor-related proteins in Wnt signal transduction. Nature 407, 530–535. 10.1038/35035117. [PubMed: 11029007]

33. Malinauskas T, and Jones EY (2014). Extracellular modulators of Wnt signalling. Current opinion in structural biology 29, 77–84. 10.1016/j.sbi.2014.10.003. [PubMed: 25460271]

34. Eubelen M, Bostaille N, Cabochette P, Gauquier A, Tebabi P, Dumitru AC, Koehler M, Gut P, Alsteens D, Stainier DYR, et al. (2018). A molecular mechanism for Wnt ligand-specific signaling. Science 361. 10.1126/science.aat1178.

35. Cho C, Wang Y, Smallwood PM, Williams J, and Nathans J (2019). Molecular determinants in Frizzled, Reck, and Wnt7a for ligand-specific signaling in neurovascular development. eLife 8. 10.7554/eLife.47300.

36. Martin M, Vermeiren S, Bostaille N, Eubelen M, Spitzer D, Vermeersch M, Profaci CP, Pozuelo E, Toussay X, Raman-Nair J, et al. (2022). Engineered Wnt ligands enable blood-brain barrier repair in neurological disorders. Science 375, eabm4459. 10.1126/science.abm4459. [PubMed: 35175798]

37. Li H, Miki T, Almeida GM, Hanashima C, Matsuzaki T, Kuo CJ, Watanabe N, and Noda M (2019). RECK in Neural Precursor Cells Plays a Critical Role in Mouse Forebrain Angiogenesis. iScience 19, 559–571. 10.1016/j.isci.2019.08.009. [PubMed: 31445376]

38. Michalak M, Groenendyk J, Szabo E, Gold LI, and Opas M (2009). Calreticulin, a multi-process calcium-buffering chaperone of the endoplasmic reticulum. The Biochemical journal 417, 651–666. 10.1042/BJ20081847. [PubMed: 19133842]

39. Jumper J, Evans R, Pritzel A, Green T, Figurnov M, Ronneberger O, Tunyasuvunakool K, Bates R, Zidek A, Potapenko A, et al. (2021). Highly accurate protein structure prediction with AlphaFold. Nature 596, 583–589. 10.1038/s41586-021-03819-2. [PubMed: 34265844]

40. Kozlov G, Pocanschi CL, Rosenauer A, Bastos-Aristizabal S, Gorelik A, Williams DB, and Gehring K (2010). Structural basis of carbohydrate recognition by calreticulin. The Journal of biological chemistry 285, 38612–38620. 10.1074/jbc.M110.168294. [PubMed: 20880849]

41. Blees A, Januliene D, Hofmann T, Koller N, Schmidt C, Trowitzsch S, Moeller A, and Tampe R (2017). Structure of the human MHC-I peptide-loading complex. Nature 551, 525–528. 10.1038/nature24627. [PubMed: 29107940]

42. Domnick A, Winter C, Susac L, Hennecke L, Hensen M, Zitzmann N, Trowitzsch S, Thomas C, and Tampe R (2022). Molecular basis of MHC I quality control in the peptide loading complex. Nature communications 13, 4701. 10.1038/s41467-022-32384-z.

43. Oliver JD, Roderick HL, Llewellyn DH, and High S (1999). ERp57 functions as a subunit of specific complexes formed with the ER lectins calreticulin and calnexin. Molecular biology of the cell 10, 2573–2582. 10.1091/mbc.10.8.2573. [PubMed: 10436013]

44. Rios-Esteves J, Haugen B, and Resh MD (2014). Identification of key residues and regions important for porcupine-mediated Wnt acylation. The Journal of biological chemistry 289, 17009–17019. 10.1074/jbc.M114.561209. [PubMed: 24798332]

45. Lee CJ, Rana MS, Bae C, Li Y, and Banerjee A (2019). In vitro reconstitution of Wnt acylation reveals structural determinants of substrate recognition by the acyltransferase human Porcupine. The Journal of biological chemistry 294, 231–245. 10.1074/jbc.RA118.005746. [PubMed: 30420431]

46. Chai G, Szenker-Ravi E, Chung C, Li Z, Wang L, Khatoo M, Marshall T, Jiang N, Yang X, McEvoy-Venneri J, et al. (2021). A Human Pleiotropic Multiorgan Condition Caused by Deficient Wnt Secretion. The New England journal of medicine 385, 1292–1301. 10.1056/NEJMoa2033911. [PubMed: 34587386]

47. Tsutsumi N, Hwang S, Waghray D, Hansen S, Jude KM, Wang N, Miao Y, Glassman CR, Caveney NA, Janda CY, et al. (2023). Structure of the Wnt-Frizzled-LRP6 initiation complex reveals the basis for coreceptor discrimination. Proceedings of the National Academy of Sciences of the United States of America 120, e2218238120. 10.1073/pnas.2218238120. [PubMed: 36893265]
48. Hoang B, Moos M Jr., Vukicevic S, and Luyten FP (1996). Primary structure and tissue distribution of FRZB, a novel protein related to Drosophila frizzled, suggest a role in skeletal morphogenesis. The Journal of biological chemistry 271, 26131–26137. 10.1074/jbc.271.42.26131. [PubMed: 8824257]
49. Mulligan KA, Fuerer C, Ching W, Fish M, Willert K, and Nusse R (2012). Secreted Wingless-interacting molecule (Swim) promotes long-range signaling by maintaining Wingless solubility. Proceedings of the National Academy of Sciences of the United States of America 109, 370–377. 10.1073/pnas.1119197109. [PubMed: 22203956]
50. Mihara E, Hirai H, Yamamoto H, Tamura-Kawakami K, Matano M, Kikuchi A, Sato T, and Takagi J (2016). Active and water-soluble form of lipidated Wnt protein is maintained by a serum glycoprotein afamin/alpha-albumin. eLife 5. 10.7554/eLife.11621.
51. Yeagle P. (2016). The membranes of cells, Third edition Edition (London : Academic Press is an imprint of Elsevier).
52. Sun J, and MacKinnon R (2020). Structural Basis of Human KCNQ1 Modulation and Gating. Cell 180, 340–347 e349. 10.1016/j.cell.2019.12.003. [PubMed: 31883792]
53. Punjani A, Rubinstein JL, Fleet DJ, and Brubaker MA (2017). cryoSPARC: algorithms for rapid unsupervised cryo-EM structure determination. Nature methods 14, 290–296. 10.1038/nmeth.4169. [PubMed: 28165473]
54. Zheng SQ, Palovcak E, Armache JP, Verba KA, Cheng Y, and Agard DA (2017). MotionCor2: anisotropic correction of bcam-induced motion for improved cryo-electron microscopy. Nature methods 14, 331–332. 10.1038/nmeth.4193. [PubMed: 28250466]
55. Zivanov J, Nakane T, Forsberg BO, Kimanius D, Hagen WJ, Lindahl E, and Scheres SH (2018). New tools for automated high-resolution cryo-EM structure determination in RELION-3. eLife 7. 10.7554/eLife.42166.
56. Rohou A, and Grigorieff N (2015). CTFFIND4: Fast and accurate defocus estimation from electron micrographs. J. Struct. Biol 192, 216–221. [PubMed: 26278980]
57. Wagner T, Merino F, Stabrin M, Moriya T, Antoni C, Apelbaum A, Hagel P, Sitsel O, Raisch T, Prumbaum D, et al. (2019). SPHIRE-crYOLO is a fast and accurate fully automated particle picker for cryo-EM. Commun. Biol 2, 218. [PubMed: 31240256]
58. Adams PD, Afonine PV, Bunkoczi G, Chen VB, Davis IW, Echols N, Headd JJ, Hung LW, Kapral GJ, Grosse-Kunstleve RW, et al. (2010). PHENIX: a comprehensive Python-based system for macromolecular structure solution. Acta crystallographica. Section D, Biological crystallography 66, 213–221. 10.1107/S0907444909052925. [PubMed: 20124702]
59. Emsley P, and Cowtan K (2004). Coot: model-building tools for molecular graphics. Acta crystallographica. Section D, Biological crystallography 60, 2126–2132. 10.1107/S0907444904019158. [PubMed: 15572765]
60. Croll TI (2018). ISOLDE: a physically realistic environment for model building into low-resolution electron-density maps. Acta Crystallogr D Struct Biol 74, 519–530. 10.1107/S2059798318002425. [PubMed: 29872003]
61. Pettersen EF, Goddard TD, Huang CC, Meng EC, Couch GS, Croll TI, Morris JH, and Ferrin TE (2021). UCSF ChimeraX: Structure visualization for researchers, educators, and developers. Protein Sci 30, 70–82. 10.1002/pro.3943. [PubMed: 32881101]
62. Pettersen EF, Goddard TD, Huang CC, Couch GS, Greenblatt DM, Meng EC, and Ferrin TE (2004). UCSF Chimera--a visualization system for exploratory research and analysis. Journal of computational chemistry 25, 1605–1612. 10.1002/jcc.20084. [PubMed: 15264254]
63. Vanommeslaeghe K, Hatcher E, Acharya C, Kundu S, Zhong S, Shim J, Darian E, Guvench O, Lopes P, Vorobyov I, and Mackerell AD Jr. (2010). CHARMM general force field: A force field for drug-like molecules compatible with the CHARMM all-atom additive biological force fields. Journal of computational chemistry 31, 671–690. 10.1002/jcc.21367. [PubMed: 19575467]

64. Brooks BR, Bruccoleri RE, Olafson BD, States DJ, Swaminathan S, and Karplus M (1983). CHARMM: A program for macromolecular energy, minimization, and dynamics calculations. Journal of computational chemistry 4, 30.

65. Li H, Robertson AD, and Jensen JH (2005). Very fast empirical prediction and rationalization of protein pKa values. Proteins 61, 704–721. 10.1002/prot.20660. [PubMed: 16231289]

66. Jo S, Kim T, Iyer VG, and Im W (2008). CHARMM-GUI: a web-based graphical user interface for CHARMM. Journal of computational chemistry 29, 1859–1865. 10.1002/jcc.20945. [PubMed: 18351591]

67. Lomize MA, Lomize AL, Pogozheva ID, and Mosberg HI (2006). OPM: orientations of proteins in membranes database. Bioinformatics 22, 623–625. 10.1093/bioinformatics/btk023. [PubMed: 16397007]

68. Jorgensen W, Chandrasekhar J, Madura J, Impey R, and Klein M (1983). Comparison of simple potential functions for simulating liquid water. The Journal of Chemical Physics 79, 9.

69. Phillips JC, Braun R, Wang W, Gumbart J, Tajkhorshid E, Villa E, Chipot C, Skeel RD, Kale L, and Schulten K (2005). Scalable molecular dynamics with NAMD. Journal of computational chemistry 26, 1781–1802. 10.1002/jcc.20289. [PubMed: 16222654]

70. MacKerell AD, Bashford D, Bellott M, Dunbrack RL, Evanseck JD, Field MJ, Fischer S, Gao J, Guo H, Ha S, et al. (1998). All-atom empirical potential for molecular modeling and dynamics studies of proteins. J Phys Chem B 102, 3586–3616. 10.1021/jp973084f. [PubMed: 24889800]

71. Essmann U, Perera L, Berkowitz ML, Darden T, Lee H, and Pedersen LG (1995). A smooth particle mesh Ewald method. J. Chem. Phys 103, 16.

**Highlights:**

- Calreticulin binds most Wnt isoforms via their N-glycan in the ER.
- Calreticulin, Porcupine, and Wntless form a complex with Wnt during Wnt biogenesis.
- A phospholipid binds to the center of Wntless, modulating Wnt association.
- RECK binds to the N-terminal domain of Wnt7a for ligand-specific signal activation.

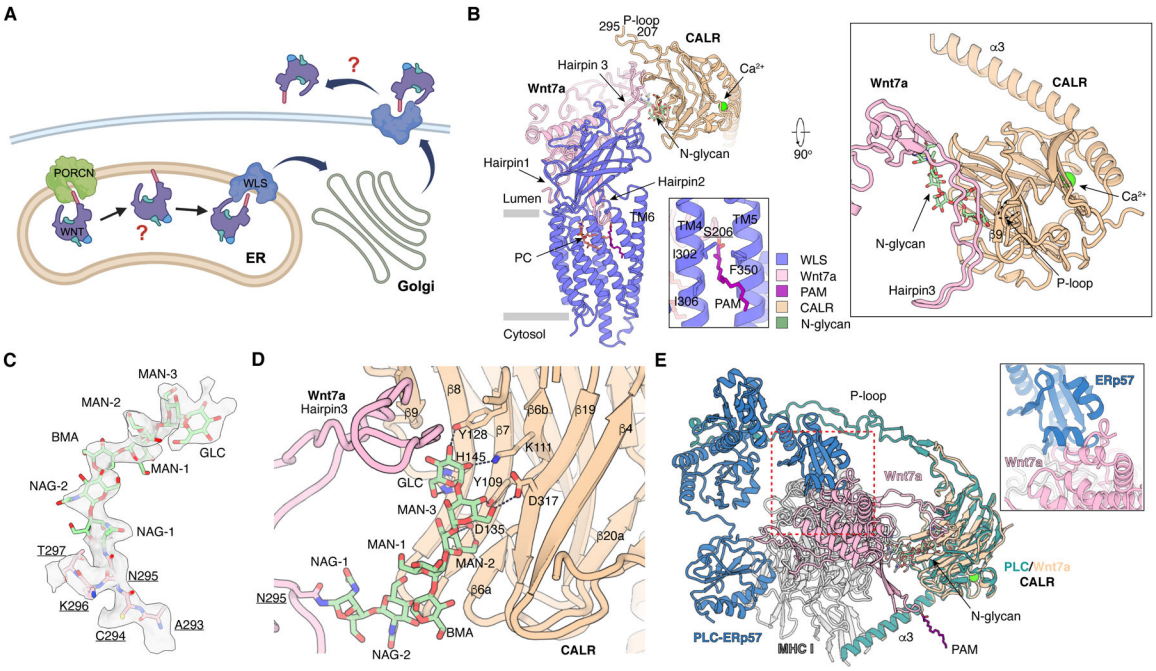


**Figure 1. Structural analysis of Wnt7a-WLS-CALR complex.**

**(A)** The general production pathway of Wnt ligands. In the ER, Wnts (purple) are modified by PORCN (green). Secretion of the modified Wnts is mediated by WLS (blue). It remains unclear how Wnts are transferred from PORCN to WLS and how Wnts are released from WLS. Created with BioRender.com.

**(B)** Overall structure of Wnt7a-WLS-CALR complex. The interaction details between PAM and WLS are indicated. The interaction area between the Wnt7a and CALR is shown in the right panel.

**(C)** Cryo-EM map of N-glycan of Wnt7a and its linked loop (contour level: 0.44).

**(D)** Interaction details between CALR and hairpin3, N-glycan of Wnt7a. The hydrophilic interactions are indicated by dashed lines.

**(E)** Structural comparison of Wnt7a-WLS-CALR complex with the PLC complex (PDB: 7QPD). The clash between Wnt7a and ERp57 is zoomed-in in the right box.

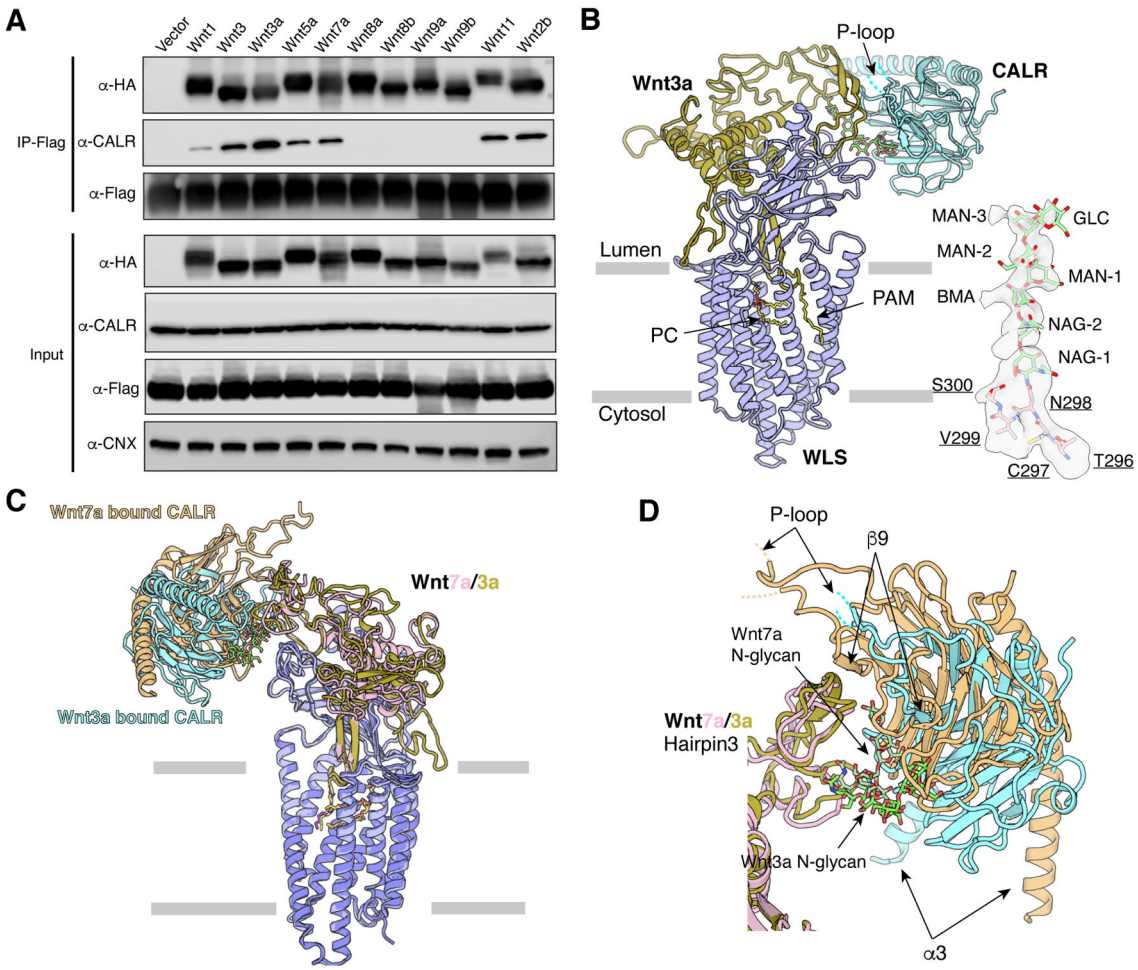


**Figure 2. Structure of Wnt3a-WLS-CALR complex.**

**(A)** Anti-Flag coimmunoprecipitation (co-IP) assays in total HEK293 cell lysates of cells which expressed C-terminal Flag-tagged WLS with C-terminal Strep-HA-tagged Wnt proteins. Endogenous CALR is associated with WLS in the presence of Wnt1/2b/3/3a/5a/7a/11, but not Wnt8a/8b/9a/9b.

**(B)** Overall structure of Wnt3a-WLS-CALR complex viewed from the side of the membrane and cryo-EM map of its N-glycan at Asn298 (contour level: 0.285).

**(C)** The comparison of the overall structures of Wnt3a-WLS-CALR complex and Wnt7a-WLS-CALR complex.

**(D)** The comparison of the CALR structures of Wnt3a-WLS-CALR and Wnt7a-WLS-CALR complexes. The shifts of the CALR structural elements and the N-glycans are indicated by arrows.

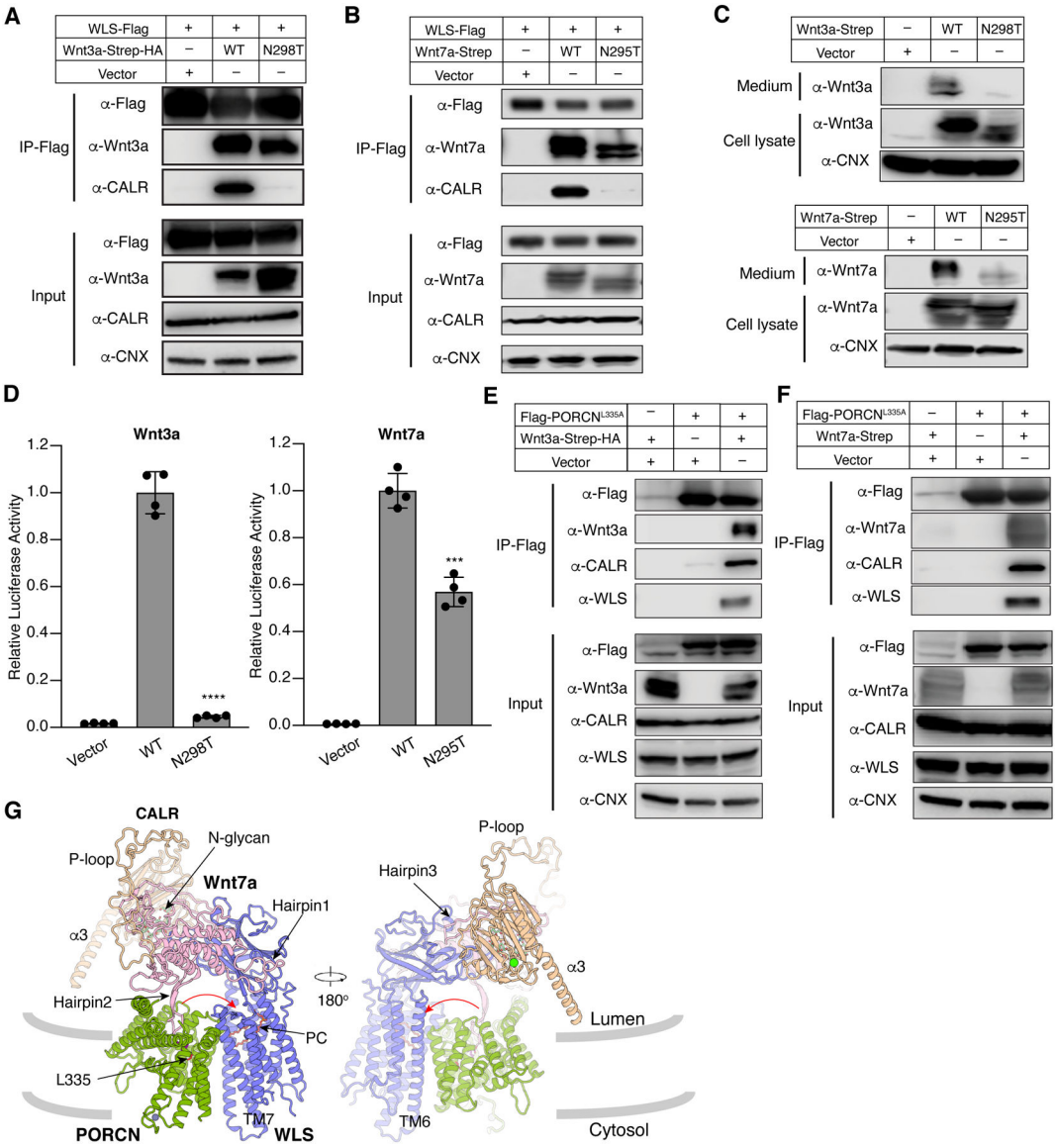


**Figure 3. Validation of the roles of CALR and the Wnt glycosylation site in Wnt production and signaling.**

**(A)** and **(B)** Anti-Flag co-IP assays in total HEK293 cell lysates of cells which expressed C-terminal Flag-tagged WLS with or without C-terminal Strep-HA-tagged Wnt3a **(A)** or Strep-tagged Wnt7a **(B)**. Endogenous CALR is coimmunoprecipitated with WLS in the presence of $Wnt3a^{WT}$ and $Wnt7a^{WT}$ but not $Wnt3a^{N298T}$ and $Wnt7a^{N295T}$.

**(C)** The secreted level of $Wnt3a^{WT}$, $Wnt7a^{WT}$, $Wnt3a^{N298T}$ and $Wnt7a^{N295T}$.

**(D)** Signaling activity for different Wnt variants. Activity was measured by TOPFlash luciferase reporter assay. Normalized activity for wild-type Wnt (WT) is taken as 100%, and activity of Wnt mutants is shown as percentage activity compared to WT. n=4 biological repeats. Data are mean ± s.d. Two-sided t-test was performed between the wild-type and mutant groups by GraphPad Prism 9. ***, $p<0.001$; ****, $p<0.0001$.

**(E)** and **(F)** Anti-Flag co-IP assays in total HEK293 cell lysates of cells which expressed N-terminal Flag-tagged $PORCN^{L335A}$ with or without C-terminal Strep-HA-tagged Wnt3a

**(E)** and Strep-tagged Wnt7a **(F)**. Endogenous CALR and WLS were coimmunoprecipitated with PORCN$^{L335A}$ in the presence of Wnt3a and Wnt7a.

**(G)** The hypothetical model of CALR in Wnt transfer from PORCN to WLS. While the hairpin 2 is inserted into PORCN for lipidation, the rest of Wnt binds to WLS under the facilitation of CALR.

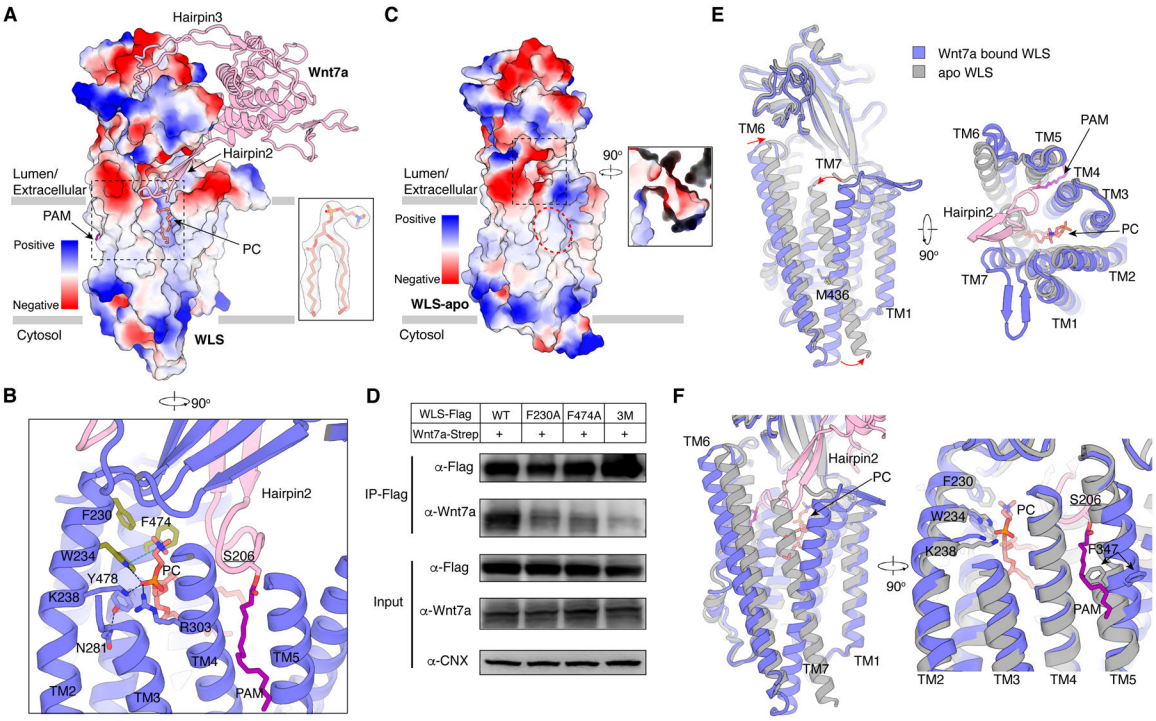


**Figure 4. Structural analysis of Wnt7a-WLS complex and the apo WLS.**

**(A)** Overall structure of Wnt7a-WLS complex. Electrostatic surface representation of WLS is shown. The cryo-EM map of putative POPC in the central cavity is shown. The central cavity opens to the extracellular/luminal leaflet and is indicated by a dashed rectangle.

**(B)** The interaction details between POPC and WLS. The residue Ser206 of Wnt7a is underlined.

**(C)** Electrostatic surface representation of the apo WLS. The closed central cavity is indicated by a red oval. A potential drug binding pocket is indicated by a dashed rectangle and zoomed-in on the right.

**(D)** Anti-Flag co-IP assays in total HEK293 cell lysates of cells which expressed C-terminal Strep-tagged Wnt7a with C-terminal Flag-tagged WLS. 3M: F230A, W234A and F474A (colored in olive green in panel **B**).

**(E)** Structural comparison between Wnt7a bound WLS (blue) and the apo WLS (gray).

**(F)** The conformational changes of TM6 and TM7 in the apo state disrupt the POPC and PAM binding.

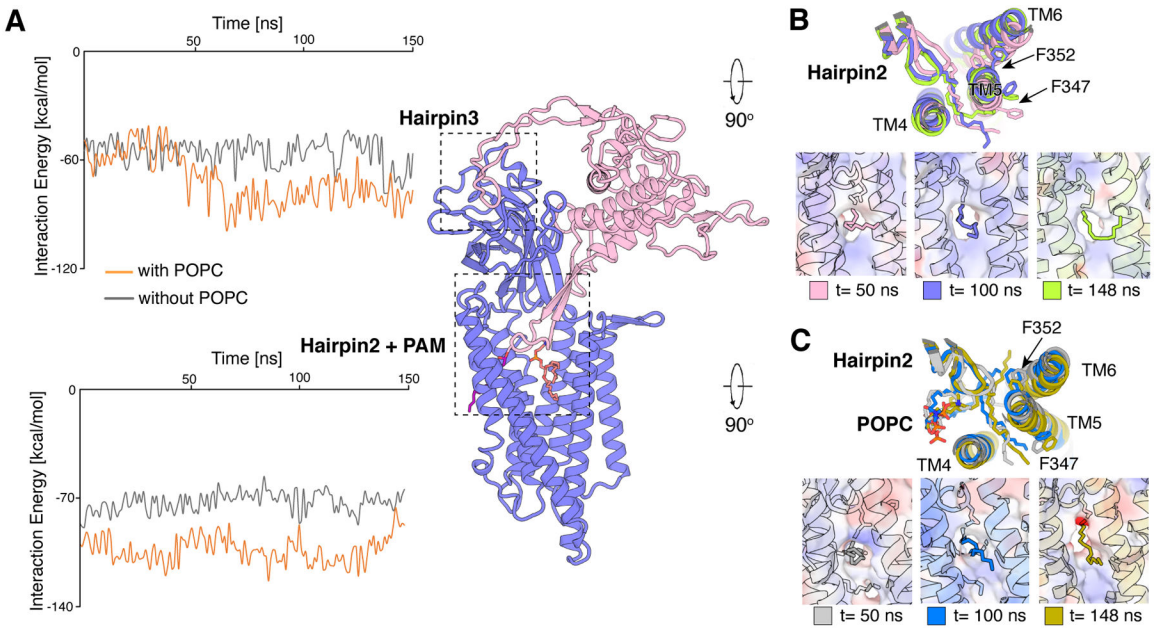


**Figure 5. The analysis of the interaction energy between WLS and Wnt7a by MD simulations at 150 ns scale.**

**(A)** The interaction energy between WLS and Wnt7a at the hairpin 3 and hairpin 2-PAM binding sites. The energy from the complex with the POPC is colored in orange and the energy from the complex without the POPC is colored in gray.

**(B)** The conformational change of TM5 without POPC at 150 ns scale. F347 and F352 rotate towards the edge of WLS and trigger the opening of cavity which accommodates the PAM. The surface representations of the PAM binding cavity from the side of the membrane are shown.

**(C)** The conformational change of TM5 with POPC at 150 ns scale. F347 and F352 retain a similar position in the presence of the POPC. The surface representations of the PAM binding cavity from the side of the membrane are shown.

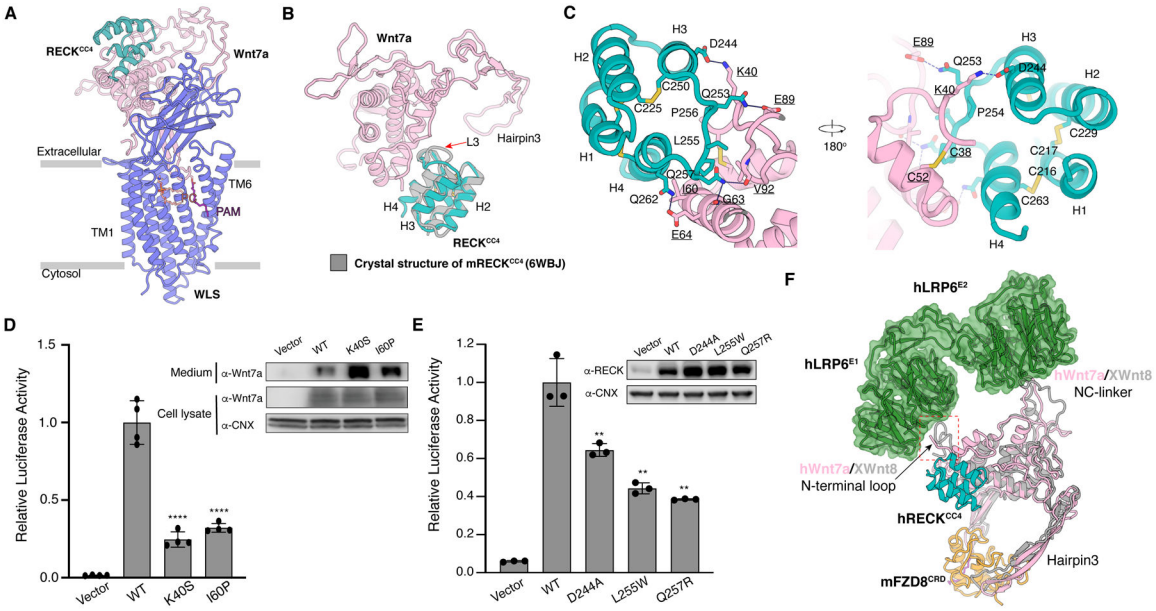


**Figure 6. Structural and functional analysis of the RECK$^{CC4}$-Wnt7a complex.**

**(A)** Overall structure of RECK$^{CC4}$-Wnt7a-WLS complex.

**(B)** Structural comparison of RECK$^{CC4}$ in the complex with Wnt7a to crystal structure of mRECK$^{CC4}$ in the apo state (PDB: 6WBJ). The conformational change of L3 loop which binds to Wnt7a is indicated by a red arrow.

**(C)** Interactions between RECK$^{CC4}$ and Wnt7a. The disulfide bonds in RECK$^{CC4}$ are indicated. The hydrophilic interactions are indicated by dashed lines.

**(D)** and **(E)** Signaling activity for Wnt7a variants **(D)** and RECK variants **(E)**. Activity was measured by TOPFlash luciferase reporter assay. Normalized activity for wild-type protein (WT) is taken as 100%, and activity of mutants are shown as percentage activity compared to WT. n=3-4 biological repeats. Data are mean ± s.d. Two-sided t-test was performed between the wild-type and mutant groups by GraphPad Prism 9. **, $p$<0.01; ****, $p$<0.0001.

**(F)** A structural model of RECK$^{CC4}$-Wnt7a-FZD8$^{CRD}$-LRP6$^{E1E2}$ complex. The structure of RECK$^{CC4}$-Wnt7a was docked to the structure of Wnt8-FZD8$^{CRD}$-LRP6$^{E1E2}$ (PDB: 8CTG).

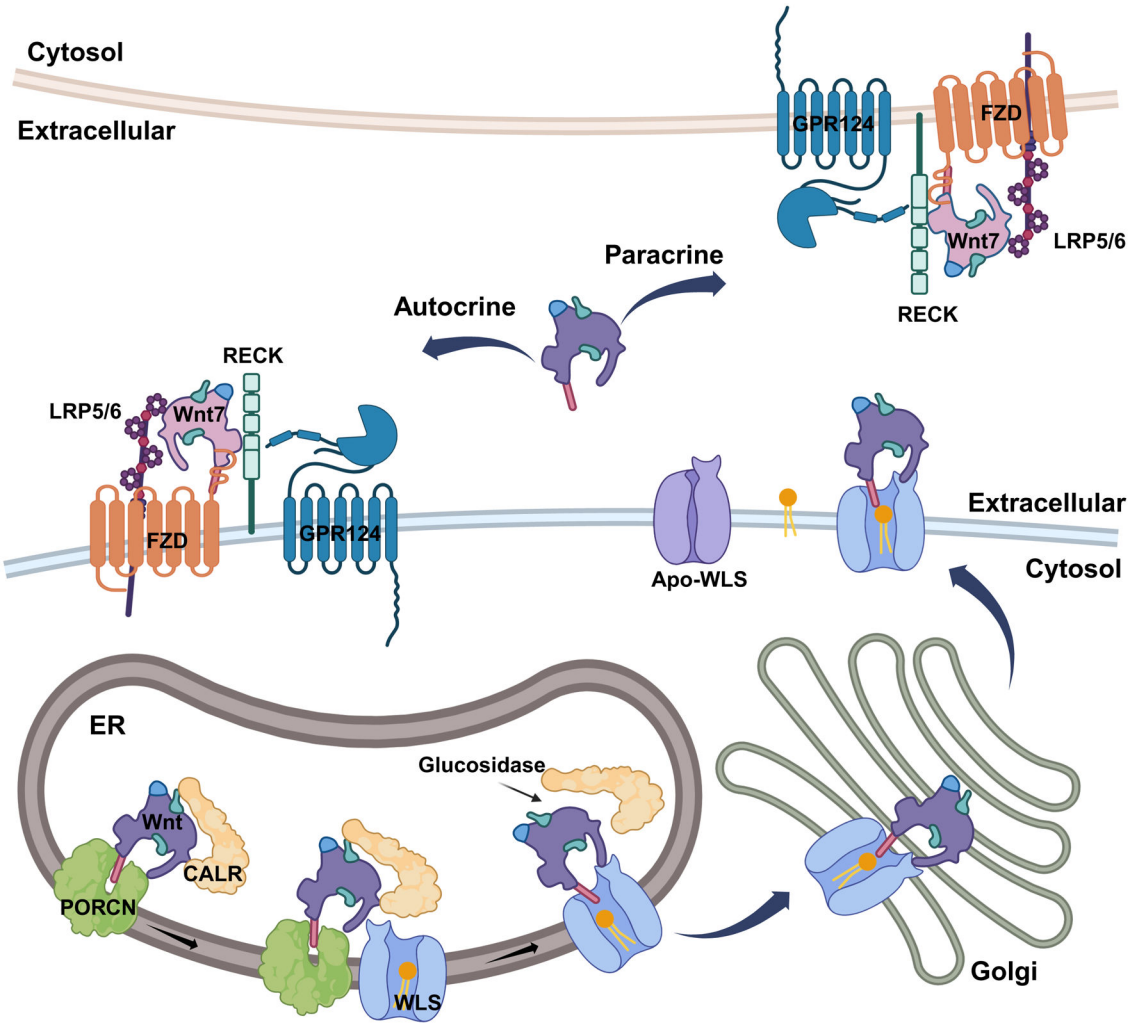


**Figure 7. Working model of Wnt production and Wnt7 specific signaling.**

The hairpin 2 of Wnt interacts with the lumen cavity of PORCN (light green) to undergo lipidation. Then, hairpins 1 and/or 3 of Wnt bind to WLS (blue), with the assistance of CALR (wheat). Once the lipidation process is complete, the hairpin 2 of Wnt dissociates from PORCN and the TMs of WLS recruit a phospholipid (yellow), which facilitates the opening of the hairpin 2 binding cavity in WLS. Then the hairpin 2 of Wnt binds to the TMs of WLS, forming a complete Wnt complex. ER-resident glucosidases will trim the sugar moiety on Wnt. At this point, CALR can disengage from the Wnt-WLS complex, allowing the complex to traffic to the Golgi apparatus. Upon reaching the cell surface, the central phospholipid may dissociate from WLS, resulting in the secretion of Wnt into the extracellular space. Outside the cell, Wnt7 can bind to FZD, and interact with the CC4 domain of RECK (green) along with other co-receptors. This interaction triggers the Wnt ligand specific signaling. Created with BioRender.com.

Key resources table

| REAGENT or RESOURCE | SOURCE | IDENTIFIER |
|---|---|---|
| **Antibodies** | | |
| Mouse monoclonal anti-FLAG tag antibody | MBL International | Cat# M185-3L; RRID: AB_11123930 |
| Rabbit monoclonal anti-Wnt7a antibody | Abcam | Cat# ab274321 |
| Rabbit monoclonal anti-Wnt3a antibody | Cell Signaling Technology | Cat# 2721S; RRID: AB_2215411 |
| Rabbit polyclonal anti-Calnexin antibody | Cell Signaling Technology | Cat# 2433S; RRID: AB_2243887 |
| Rabbit monoclonal anti-Calreticulin antibody | Cell Signaling Technology | Cat# 12238S; RRID: AB_2275208 |
| Rabbit monoclonal anti-RECK antibody | Thermo Scientific | Cat# MA5-14781; RRID: AB_11005172 |
| Rabbit Polyclonal anti-WLS (GPR177) antibody | Thermo Scientific | Cat# 50-173-1894 |
| Rabbit monoclonal anti-HA antibody | Cell Signaling Technology | Cat# 3724S; RRID: AB_1549585 |
| Anti-Rabbit IgG, HRP-linked antibody | Cell Signaling Technology | Cat# 7074S; RRID: AB_2099233 |
| Anti-mouse IgG, HRP-linked antibody | Cell Signaling Technology | Cat# 7076S; RRID: AB_330924 |
| **Bacterial and Virus Strains** | | |
| *E. coli* DH5α Competent Cells | GoldBio | Cat# CC-101-TR |
| *E. coli* DH10Bac Competent Cells | Thermo Fisher | Cat# 10361012 |
| **Chemicals, Peptides, and Recombinant Proteins** | | |
| LB broth | Fisher Scientific | Cat# BP1426-500 |
| Sf-900 III SFM medium | Gibco | Cat# 12658027 |
| Freestyle 293 expression medium | Gibco | Cat# 12338018 |
| DMEM/F12 50/50 Mix medium | Corning | Cat# 10-090-CV |
| Fetal Bovine Serum (FBS) | Cytiva | Cat# SH30396.03 |
| Penicillin-Streptomycin solution (100x) | Corning | Cat# 30-002-CI |
| HEPES | Gibco | Cat# 11344041 |
| NaCl | Fisher Scientific | Cat# S271 |
| Sodium butyrate | Millipore-Sigma | Cat# 303410 |
| Phenylmethylsulfonyl fluoride (PMSF) | GoldBio | Cat# P-470-25 |
| Leupeptin | vivitide | Cat# ILP-4041 |
| Lauryl maltose neopentyl glycol (LMNG) | Anatrace | Cat# NG310 |
| Digitonin | Thermo Scientific | Cat# 407560050 |
| Ni-NTA agarose | Qiagen | Cat# 30250 |
| Anti-Flag M2 resin | Millipore-Sigma | Cat# A2220 |
| 3X Flag peptide | ApexBio | Cat# A6001 |
| FuGENE 6 transfection reagent | Promega | Cat# E2692 |
| Cellfectin II reagent | Gibco | Cat# 10362-100 |
| PEI Max | Polysciences | Cat# 24765-1 |
| Phosphate buffered saline with Tween 20 (PBST) | Millipore-Sigma | Cat# 08057-100TAB-F |
| BS3 (bis(sulfosuccinimidyl)suberate) | Thermo Scientific | Cat# 21586 |
| Glutaraldehyde solution | Sigma-Aldrich | Cat#G5882 |

| REAGENT or RESOURCE | SOURCE | IDENTIFIER |
|---|---|---|
| Bafilomycin A1 | Fisher Scientific | Cat#NC1351384 |
| **Critical Commercial Assays** | | |
| Dual-Luciferase Reporter Assay System | Promega | Cat# E1910 |
| **Deposited Data** | | |
| Cryo-EM structure of WLS-Wnt7a-CALR | This paper | PDB: 8TZO; EMDB: EMD-41764 |
| Cryo-EM structure of WLS-Wnt3a-CALR | This paper | PDB: 8TZR; EMDB: EMD-41767 |
| Cryo-EM structure of WLS-Wnt7a-RECK$^{CC4}$ | This paper | PDB: 8TZP; EMDB: EMD-41765 |
| Cryo-EM structure of WLS | This paper | PDB: 8TZS; EMDB: EMD-41768 |
| **Experimental Models: Cell Lines** | | |
| Sf9 insect cell | ATCC | Cat# CRL-1711; RRID: CVCL_0549 |
| HEK-293S GnTI$^{-}$ | ATCC | Cat# CRL-3022; RRID: CVCL_A785 |
| SuperTopFlash HEK293 | ATCC | Cat# CRL-3249; RRID: CVCL_AQ26 |
| **Recombinant DNA** | | |
| pEG-BacMam-Wnt7a-strep | This paper | N/A |
| pEG-BacMam-Wnt3a | This paper | N/A |
| pEG-BacMam-Wnt3a-strep | This paper | N/A |
| pEG-BacMam-Flag-PORCN$^{L335A}$ | This paper | N/A |
| pEG-BacMam-CALR-8His | This paper | N/A |
| pEG-BacMam-Wnt1-Strep-HA | This paper | N/A |
| pEG-BacMam-Wnt2b-Strep-HA | This paper | N/A |
| pEG-BacMam-Wnt3-Strep-HA | This paper | N/A |
| pEG-BacMam-Wnt3a-Strep-HA | This paper | N/A |
| pEG-BacMam-Wnt5a-Strep-HA | This paper | N/A |
| pEG-BacMam-Wnt7a-Strep-HA | This paper | N/A |
| pEG-BacMam-Wnt8a-Strep-HA | This paper | N/A |
| pEG-BacMam-Wnt8b-Strep-HA | This paper | N/A |
| pEG-BacMam-Wnt9a-Strep-HA | This paper | N/A |
| pEG-BacMam-Wnt9b-Strep-HA | This paper | N/A |
| pEG-BacMam-Wnt11-Strep-HA | This paper | N/A |
| pEZT-BM | Addgene | Cat# 74099 |
| pEZT-BM-WLS-Flag | This paper | N/A |
| pRL-SV40 *Renilla* luciferase | Promega | Cat# E2231 |
| pcDNA3.1 | Invitrogen | Cat# V79020 |
| pcDNA3.1-wnt7a-strep | This paper | N/A |
| pcDNA3.1-wnt3a | This paper | N/A |
| pcDNA3.1-FZD4 | This paper | N/A |
| pcDNA3.1-RECK | This paper | N/A |
| pcDNA3.1-GPR124 | This paper | N/A |
| pHL-sec-LRP6 | This paper | N/A |

| REAGENT or RESOURCE | SOURCE | IDENTIFIER |
|---|---|---|
| pHL-sec-RECK$^{CC4}$(206-270) | This paper | N/A |
| **Software and Algorithms** | | |
| MotionCor2 | Zheng et al.[54] | https://emcore.ucsf.edu/ucsf-motioncor2 |
| CTFFIND4 | Rohou and Grigorieff[56] | http://grigoriefflab.janelia.org/ctffind4 |
| RELION 3.1 | Zivanov et al.[55] | https://www3.mrc-lmb.cam.ac.uk/relion/ |
| SPHIRE-crYOLO v1.7.6 | Wagner et al.[57] | http://sphire.mpg.de/ |
| cryoSPARC v3.3.1 cryoSPARC v4.1.1 | Punjani et al.[53] | https://cryosparc.com/ |
| UCSF Chimera 1.13 | Pettersen et al.[62] | http://www.cgl.ucsf.edu/chimera |
| UCSF ChimeraX 1.5 | Pettersen et al.[61] | https://www.cgl.ucsf.edu/chimerax/ |
| ISOLDE 1.4 | Croll[60] | https://isolde.cimr.cam.ac.uk |
| Coot 0.9.6 | Emsley et al.[59] | https://www2.mrc-lmb.cam.ac.uk/personal/pemsley/coot/ |
| Phenix 1.16 | Adams et al.[58] | http://www.phenix-online.org/ |
| PyMOL 2.3.4 | Schrödinger | https://pymol.org/2/ |
| Prism 9 | GraphPad | https://www.graphpad.com/ |
| Avogadro | Avogadro Chemistry | https://avogadro.cc/ |
| CHARMM | Brooks et al.[64] | https://www.charmm.org/ |
| PROPKA | Li et al.[65] | https://github.com/jensengroup/propka |
| NAMD | Phillips et al.[69] | http://www.ks.uiuc.edu/Research/namd/ |
| **Other** | | |
| Blue Sepharose High Performance | GE Healthcare | Cat# 90100374 |
| R1.2/1.3 400 mesh Au holey carbon grids | Quantifoil | Cat# 1210627 |
| Superose 6 Increase 10/300 GL column | Cytiva | Cat# 29091596 |
| Superdex 200 Increase 10/300 GL column | Cytiva | Cat# 28990944 |